An inter-comparison study on the impact of atmospheric boundary layer height on gigawatt-scale wind plant performance

Stefan Ivanell[1], Warit Chanprasert[1], Luca Lanzilao[2], James Bleeg[3], Johan Meyers[2], Antoine Mathieu[4,5], Søren Juhl Andersen[6], Rem-Sophia Mouradi[4,5], Eric Dupont[4,5], Hugo Olivares-Espinosa[1], and Niels Troldborg[7]

[1]Uppsala University, Department of Earth Sciences, Wind Energy Division, 621 67 Visby, Sweden
[2]KU Leuven, Department of Mechanical Engineering, Celestijnenlaan 300 – box 2421, B-3001 Leuven, Belgium
[3]DNV, One Linear Park, Avon St. Temple Quay, Bristol BS2 0PS, UK
[4]EDF R&D, 6 Quai Watier, 78400 Chatou, France
[5]CEREA, École des Ponts, Île-de-France
[6]DTU, Department of Wind and Energy Systems, Koppels Allé 403, 2800 Kgs Lyngby, Denmark
[7]DTU, Department of Wind and Energy Systems, Frederiksborgvej 399, 4000 Roskilde, Denmark

Correspondence: Stefan Ivanell (stefan.ivanell@geo.uu.se)

Abstract.

The height of the atmospheric boundary layer (ABL) exerts a significant influence on flow behavior within wind farms and directly impacts their performance. This study investigates how variations in ABL height and capping inversion layer thickness affect the efficiency and power output of a gigawatt-scale wind farm. Five advanced numerical approaches, ranging from high-fidelity large-eddy simulations (LES) to Reynolds-averaged Navier-Stokes (RANS), are used to model farm-scale flow dynamics under shallow ($\sim 150m$) and deep ($\sim 500m$) ABL conditions. The results consistently show that shallow ABLs increase flow blockage and turbine wake interactions, leading to reduced power production. In contrast, deeper ABLs promote enhanced wake recovery and increased overall energy yield. These trends were observed across all solvers, demonstrating the robustness of the findings. Notably, while some quantitative differences emerged depending on modeling fidelity and computational domain size, the overarching trends remained consistent among the participating research institutions and industry partners. The simulation cases performed are complex, and the results of the different methods show a variation of up to 10 $\%$ and further research is needed to limit this gap. Based on these results, it is not clear to what extent the variation depends on the fidelity level of the models used. The study concludes that ABL height and stability are critical parameters to consider in wind energy siting and turbine layout design to optimize performance across varying atmospheric conditions.

1 Introduction

The interaction between atmospheric winds and utility-scale wind turbines is becoming more complex as the height and rotor diameter of modern turbines increase, especially for an offshore site (Veers et al., 2019). When these turbines are clustered together into farms, the interaction with the atmosphere and atmospheric boundary layer (ABL) becomes even more intricate.

The atmospheric boundary layer (ABL) is the region in the troposphere closest to the ground, in which the flow is experiencing frictional forces due to interactions with the Earth's surface. The ABL is a highly turbulent flow region, and although various definitions exist, its height is usually identified using the location above which turbulent stresses disappear. In neutrally and unstably stratified ABLs, the turbulent region is typically capped by a strong temperature inversion (a region in which the potential temperature increases significantly over a few hundred meters), also known as a capping inversion (Stull, 1988). In stable boundary layers, a residual non-turbulent neutral layer may exist between the top of the turbulent boundary layer and the capping inversion. Both capping inversion, as well as stable stratification in the free atmosphere above (driven by global circulation), can have a significant impact on wind farm performance (Smith, 2010; Allaerts and Meyers, 2017, 2018a). In the current study, we present an inter-comparison study that investigates the effect of the height of this capping inversion on wind farms. We do this for a set of conventionally neutral boundary layers (with conditions derived from Lanzilao and Meyers, 2024), so that the height of the boundary layer effectively coincides with the height of the capping inversion.

Wind farm performance is influenced by wake and blockage effects. Wake effects have been extensively studied for many years using both numerical and experimental methods (Porté-Agel et al., 2020). Research on wind farm blockage is much more recent, and has been largely triggered by field observations reported in Bleeg et al. (2018). In this study, a significant slow-down was observed upstream of a series of wind farms by comparing pre- and post-construction measurements from available met masts, suggesting that the wind farm as a whole is blocking the flow. Two main root causes have been investigated to explain this blockage effect. A first set of studies has tried to explain the blockage as a purely hydrodynamic effect resulting from the cumulative induction of all turbines in the farm (see, e.g., Meyer Forsting et al., 2023, and references therein). A second set of studies have associated blockage with the presence of a capping inversion and lighter air in the free atmosphere above, with perturbations of the height of the boundary layer by the wind farm leading to hydrostatic changes of the pressure in the boundary layer, and the excitation of gravity waves on the inversion layer and in the free atmosphere above (Smith, 2010; Allaerts and Meyers, 2017, 2018a). Recently, Lanzilao and Meyers (2024, 2022) managed to separate both effects, showing for a range of existing atmospheric conditions over the North Sea, that the hydrostatic blockage effect is an order magnitude larger than the hydrodynamic component (Lanzilao and Meyers, 2024), though both in principle co-exist in the presence of a capping inversion and free-atmosphere stratification. The stratification not only enhances the adverse pressure gradients, i.e., increased pressure in the flow direction, and associated wind speed decreases upstream of a wind farm, it also, in turn, increases the pressure drop from the front to the back of the wind farm, enhancing wake recovery and influencing turbine power production throughout the array (Lanzilao and Meyers, 2024).

With the recognition of the importance of free-atmosphere stratification for wind farm flows, and the challenges that arise in correctly predicting the pressure field, which is tightly linked to the excitation of gravity waves and a correct set-up of boundary conditions in simulations (Lanzilao and Meyers, 2023), it is of interest to compare the performance of widely used numerical solvers among the wind industry and researchers for wind farm flow cases that are subject to significant hydrostatic effects and gravity waves. In the current study, we compare five such solvers, three that are using a large-eddy simulation framework, and two that are using Reynolds-averaged Navier-Stokes simulation framework. We consider a fixed, densely spaced, wind farm

(in which blockage effects are expected to be high), and compare the performance of the different simulation tools for two different ABL (/capping inversion) heights, next to also looking at the effect of the capping inversion thickness.

2 Numerical Setup

In this section, an overview of the simulation cases and the numerical setup for different solvers is presented. Conventionally Neutral Atmospheric Boundary Layers (CNBL) with different BLHs are considered in this study. The boundary layer initialization follows Lanzilao and Meyers (2024) where the initial velocity and potential temperature profiles are generated using the Zilitinkevich (1989) and Rampanelli and Zardi (2004) models, respectively. The Geostrophic wind (U_G) is set to 10 m/s with a surface roughness (z_0) of 1×10^{-4} m. The surface heat flux at the bottom surface is zero according to the CNBL definition.

The BLHs of 150 and 500 m are investigated. These heights are prescribed by the capping inversion height with a strength ($\Delta\theta$) of 5 K. Moreover, two different capping-inversion thickness ΔH values are considered, i.e., 100 and 500 m, for the BLH of 500 m. A free lapse rate (Γ) of 4 K/km is applied above the inversion layer. The latitude is set to 55.0°, which represents the latitude of the Doggers Bank offshore wind farm in the North Sea. For reference, the Froude number ($Fr = U_B/\sqrt{g'H}$) and the P_N number ($P_N = U_B^2/NU_GH$) have been estimated, where U_B is the bulk velocity, calculated from the planar-averaged wind speed in the streamwise direction along the boundary layer height; g' is the reduced gravity ($g' = g\Delta\theta/\theta_0$); $N = \sqrt{g\Gamma/\theta_0}$ is the Brunt–Väisälä frequency; and H is the boundary layer height (Lanzilao and Meyers, 2024). For the boundary layer height of 150 m, the Fr and P_N numbers are on the order of 1.9 and 5.5, respectively. For a height of 500 m, the values are approximately 1.1 and 1.8, respectively. The parameters for each case are summarized in Table 1.

Table 1. Case Definition Summary

Case	H [m]	$\Delta\theta$ [K]	ΔH [m]	Γ [K/km]
H150	150	5	100	4
H500	500	5	100	4
H500-dh500	500	5	500	4

The wind farm consists of 100 IEA 15 MW reference turbine (Gaertner et al., 2020) arranged in a 10×10 staggered layout with 5D spacing in both streamwise and spanwise directions as shown in Fig. 1 resulting in a farm length and width of $L_x^f = 10.8$ and $L_y^f = 11.4$ km where the x, y and z axes refer to the streamwise, spanwise and vertical directions, respectively. The turbine has a rotor diameter (D) of 240 m and a hub height (HH) of 150 m.

There are five participants from industry and academia including DNV, Danmarks Tekniske Universitet (DTU), Electricité de France (EDF), Katholieke Universiteit Leuven (KUL), and Uppsala Universitet (UU). The name and type of numerical solvers for each institution, as well as turbine representations, are listed in Table 2.

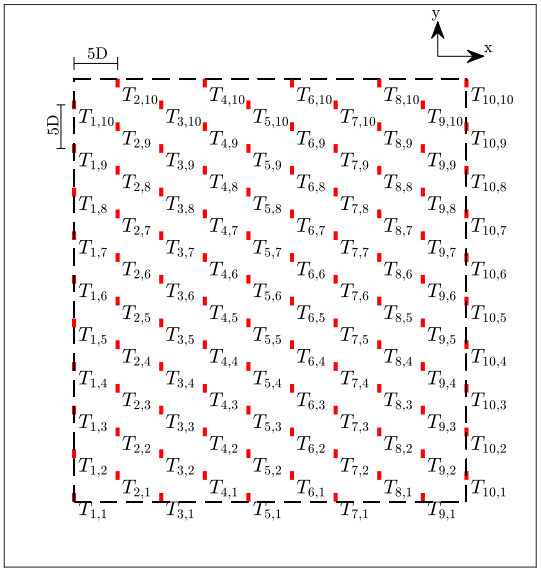

Figure 1. The layout of an idealized wind farm used in this study. Turbines are marked with a letter T and the subscript numbers indicate the row and column, respectively. The x-axis refers to the streamwise direction.

Table 2. List of Participants

Partner	Model Type	Solver Name	Turbine Modelling
DNV	RANS	STAR-CCM+	Rotating ADM
DTU	LES	EllipSys3D	Rotating ADM coupled to HAWC2
EDF	RANS	code_saturne	Non-rotating ADM
KUL	LES	SP-Wind	Non-rotating ADM
UU	LES	SOWFA	Rotating ADM

Statistical calculations for the turbulent flow and turbine output of the transient flow solvers are conducted over a physical simulation period of at least one hour. It should be noted that DTU and UU did not perform the simulation for the H500-dh500 case.

The details of numerical setup for each solver, such as computational domain and mesh resolutions, boundary conditions, numerical schemes and turbine modeling, are provided in the following subsections.

2.1 DNV STAR-CCM+ Setup

STAR-CCM+ is a general purpose simulation software package best known for computational fluid dynamics. Within STAR-CCM+, DNV customized a steady-state RANS model for simulation for wind farm flows. The turbulence closure is standard $k-\varepsilon$ with modified coefficients. The direct influence of buoyancy on the mean flow is simulated via a shallow Boussinesq

formulation; extra terms in the closure equations represent the influence of buoyancy on turbulence. Coriolis terms are in the momentum equation. The turbines are represented with a simple actuator disk model where the body forces are functions of the average axial-component of velocity across the disk. These functions derive from the IEA 15 MW power and thrust curves, defined as functions of hub-height freestream wind speed, using the procedure described in Bleeg and Montavon (2022). More information on this flow model may be found in Bleeg et al. (2018).

The simulations in this study were run within a domain of size 66 km x 66 km x 17 km. The wind farm is located 40 km downstream of the inflow boundary. The mesh spacing is 12 m around each actuator disk and 24 m around the wind farm.

Vertical inflow profiles are generated using a steady-state 1D, single column precursor simulation with the input potential temperature profile frozen. After the steady-state simulation converges, the potential temperature is unfrozen and the 1D solution is marched in time to confirm the full set of profiles are in quasi-equilibrium.

2.2 DTU EllipSys3D Setup

EllipSys3D solves the incompressible Navier–Stokes equations in general curvilinear coordinates using a finite volume method in multi-block structure Michelsen (1992, 1994); Sørensen (1995). Rhie-Chow interpolation is applied to prevent pressure decoupling, which is solved using an improved version of the SIMPLEC algorithm (Shen et al., 2003). The convective terms are discretized using a fourth-order central difference scheme which includes an artificial viscosity term to suppress numerical wiggles (Wit and van Rhee, 2013), and time stepping is second-order with subiterations. Several RANS and LES turbulence models are implemented in EllipSys3D, where the anisotropic mimimal dissipation (AMD) Abkar et al. (2016) model has been utilized in the current simulations. Rayleigh damping is applied at high altitudes ($> 1000m$).

Initially, a precursor is simulated to spin up the CNBL. The precursor is performed in a domain $L_x \times L_y \times L_z = 10,240$ m $\times 10,240$ m $\times 3,000$ m with a total of $N_x \times N_y \times N_z = 512 \times 512 \times 384 \approx 100 \cdot 10^6$ cells corresponding to mesh resolution of $\Delta x \times \Delta y \times \Delta z = 20$ m $\times 20$ m $\times 5$ m in the streamwise, lateral, and vertical direction. The equidistant mesh in the vertical is maintained at an altitude of $1,500$m after which the cells are stretched. Cyclic boundary conditions are imposed in the streamwise and lateral direction, while a wind direction controller is imposed to continuously adjust the wind direction at $z = 150$ m to ensure that the flow direction is aligned with the wind turbines at hub height (Sescu and Meneveau, 2014; Allaerts and Meyers, 2015). The precursor is initially spun up for 20 hours after which cross-stream planes are extracted for a total duration of 2 hours.

Subsequently, a mesh is build for the successor, which is $L_x \times L_y \times L_z = 30,000$ m $\times 30,000$ m $\times 3,000$ m with a total of $N_x \times N_y \times N_z = 512 \times 448 \times 192 \approx 44 \cdot 10^6$ cells. The mesh has a central equidistant region of $L_{x,equi} \times L_{x,equi} \times L_{x,equi} = 13,530$ m $\times 12,120$ m $\times 1,500$ with $\Delta x \times \Delta y \times \Delta z = 30$ m $\times 30$ m $\times 10$ m in the streamwise, lateral, and vertical directions with cells stretched to the boundaries. The precursor planes have been repeated to cover the extended domain of the successor simulations. The wind turbines are modeled by applying body forces in EllipSys3D, which is fully coupled to the aero-elastic tool HAWC2 (Larsen and Hansen, 2007) through the Dynamiks interface[1]. Velocities are transferred from EllipSys3D to HAWC2, which calculates aerodynamic forces and deflections, which are transferred back to EllipSys3D (Sørensen et al.,

[1]https://dynamiks.pages.windenergy.dtu.dk/dynamiks/index.htmlhttps://dynamiks.pages.windenergy.dtu.dk/dynamiks/index.html

2015; Hodgson et al., 2022, 2023). HAWC2 also contains a dynamic torque controller, which enables the turbines to respond to the dynamically changing inflow by dynamically updating pitch and rotational speed, but it does not yaw the turbines. The impact of realistic and dynamic wind turbine controllers has been shown to have a significant influence on power production for wind farms (Troldborg and Andersen, 2023). Turbines can be modeled as actuator lines (Sørensen and Shen, 2002) or as actuator disks (Mikkelsen, 2004), which is used in this study. The simulations are run for 2 hours, where the initial 1 hour transient is discarded as the flow is still developing.

2.3 EDF code_saturne Setup

The CFD code code_saturne, primarily developed by EDF, is an open-source, free-to-use finite volume CFD solver for the Navier-Stokes equations. It can manage scalar transport for various types of flows - 2D, 2D-axisymmetric, and 3D, steady or unsteady, laminar or turbulent, incompressible, dilatable, weakly compressible, or isothermal. Code_saturne comes with modules specifically designed for certain physics, such as atmospheric flows. Extensive explanation of its modeling capabilities, including the atmospheric module, can be found in code_saturne's v8.0 online theory guide (https://www.code-saturne.org/documentation/8.0/theory.pdf).

Reynolds Averaged Navier Stokes (RANS) with linear production $k-\varepsilon$ closure (Guimet and Laurence, 2002) is used to model the turbulence. The presence of wind turbines is accounted for using a non-rotating ADM with a constant body force function of the disk-averaged velocity and yaw control.

Wind farm simulations with code_saturne are performed in two steps. The first step consists of a 1D bi-periodic single column precursor simulation to generate quasi-steady inflow profiles for the velocity, temperature and turbulent quantities. The second step consists of the full 3D farm simulation in a circular domain with refined grid in the farm and around turbines. The numerical domain is 25 km high and a diameter as large as 4.7 times the length of the longest diagonal of the farm was shown to be sufficient to avoid confinement effects. Damping layers at the top and at lateral boundaries are implemented to prevent the reflection of gravity waves.

2.4 KUL SP-Wind Setup

The SP-Wind flow solver is an in-house software developed over the past 15 years at KU Leuven (Meyers and Sagaut, 2007; Calaf et al., 2010). In the current study, we use this software for solving the filtered Navier–Stokes equations with Boussinesq approximation coupled with a transport equation for the potential temperature to investigate the flow in and around a large-scale wind farm (Allaerts and Meyers, 2017; Lanzilao and Meyers, 2022, 2023). Here, we adopt the same solver version used by Lanzilao and Meyers (2024), which is described below.

The governing equations are integrated in time using a classic fourth-order Runge-Kutta scheme, with the time step determined by a Courant-Friedrichs-Lewy (CFL) number of 0.4. The streamwise (x) and spanwise (y) directions are discretized using a Fourier pseudo-spectral method. This approach involves discretizing all linear terms in the spectral domain while performing non-linear operations in the physical domain, which reduces the computational cost of convolutions from quadratic to log-linear (Fornberg, 1996). Additionally, the 3/2 dealiasing technique from Canuto et al. (1988) is employed to prevent

aliasing errors. For the vertical dimension (z), an energy-preserving fourth-order finite difference scheme is utilized (Verstappen and Veldman, 2003). The impact of subgrid-scale motions on the resolved flow is modeled using the stability-dependent Smagorinsky model (Stevens et al., 2000), with the Smagorinsky coefficient C_s set to 0.14. Near the wall, this coefficient is damped using the function proposed by Mason and Thomson (1992). Continuity is maintained by solving the Poisson equation at each stage of the Runge-Kutta scheme. We refer to Delport (2010) for more details on the discretization of the continuity and momentum equations while the implementation of the thermodynamic equation and sub-grid scale model are explained in detail in Allaerts (2016).

The flow solver adopts two numerical domains simultaneously marched in time: the precursor and main domains. The precursor domain, which does not contain turbines, has the function of generating a fully developed, statistically steady turbulent flow. This flow is then used to drive the simulation in the main domain. Following the approach in Allaerts and Meyers (2017, 2018a) and Lanzilao and Meyers (2024), the precursor domain dimensions are set to $L_x^p = L_y^p = 10$ km and $L_z^p = 3$ km. The wind farm is situated in the main domain, which must be sufficiently large to avoid artificial effects from domain boundaries. Lanzilao and Meyers (2024) have shown that the width of the numerical domain can significantly alter the numerical results. To this end, we fix the main domain size to $L_x \times L_y = 50 \times 40$ km^2, which leads to a domain-to-farm width ratio of 3.51. Consistent with previous studies, the main domain height is set to $L_z = 25$ km (Allaerts and Meyers, 2017, 2018a; Lanzilao and Meyers, 2022, 2023, 2024). This vertical extent allows gravity waves to dissipate and radiate energy outward, minimizing reflectivity. After completing the precursor spin-up phase, the precursor domain width and height are extended to match the main domain dimensions, using the method described in Sanchez Gomez et al. (2023) and Lanzilao and Meyers (2024). To reach a statistically steady state, the flow fields in the precursor simulation are marched in time for 20 h. These flow fields are used to drive the main domain, where a second spin-up phase of 1 h takes place so that the flow adjusts to the presence of the turbines. Next, the wind-angle controller which keeps the flow aligned with the streamwise direction at hub height is switched off and statistics are collected over a time window of 2 h.

In regard to the grid resolution, we fix $\Delta x = 31.25$ m and $\Delta y = 21.74$ m in the streamwise and spanwise direction, respectively. This leads to $N_x = 1600$ and $N_y = 1840$ grid points for the main domain and to $N_x^p = 160$ and $N_y^p = 230$ points for the precursor domain. In the vertical direction, we adopt a stretched grid which corresponds to the one used in Lanzilao and Meyers (2022, 2023, 2024), i.e. with a resolution of 5 m within the first 1.5 km and stretched above, for a total of 490 grid points. The combination of precursor and main domains leads to a total of roughly 6.92×10^9 degrees of freedom (DOF).

At the top of the domain, we use the Rayleigh damping layer (RDL) to minimize gravity-wave reflection (Klemp and Lilly, 1977). To avoid periodicity in the streamwise direction, we adopt the wave-free fringe-region technique developed by Lanzilao and Meyers (2023). The buffer layers set-up corresponds to the one previously used by Lanzilao and Meyers (2024). Hence, the RDL is 10 km thick and is located between $z = 15$ km and $z = 25$ km. Moreover, $\nu^{\mathrm{ra}} = 5.15$ and $s^{\mathrm{ra}} = 3$ are parameters used in the RDL. The fringe region is 5.5 km long and is located at the end of the main domain. Further, we set $x_s^h = L_x - L_x^{\mathrm{fr}}$, $x_e^h = L_x - 2.8$ km and $\delta_s^h = \delta_e^h = 0.4$ km while $x_s^d = x_s^h$, $x_e^d = L_x$, $\delta_s^d = 2.5$ km and $\delta_e^d = 3$ km. Finally, we fix the strength of the forcing to $h_{\max} = 0.3$ s^{-1}.

The turbine drag force is represented with the non-rotating actuator disk model (Calaf et al., 2010), where the power is computed as the product between the thrust force and the turbine disk velocity. We use a constant thrust coefficient value of 0.778, which corresponds to a C_T' of 1.44. A simple yaw controller is implemented to keep the turbine-rotor disks perpendicular to the incident wind flow measured one rotor diameter upstream.

2.5 UU SOWFA Setup

SOWFA (Simulator fOr Wind Farm Applications) was developed by NREL (Churchfield et al., 2012). It is built on the OpenFOAM software, an open source finite-volume solver that can be coupled to an aeroelastic code for turbine load and control study. Turbulent winds and wakes are modeled using LES with the one-equation eddy viscosity subgrid-scale model (Deardorff, 1980).

The domain extent is set to $L_x \times L_y \times L_z = 26400$ m $\times 32000$ m $\times 6000$ m with a mesh resolution of $\Delta x \times \Delta y \times \Delta z = 20$ m $\times 20$ m $\times 8$ m up to a height of 720 m. The mesh generation was carried out by dividing the domain into four horizontal layers, with the mesh vertically stretched and a larger expansion ratio applied to the upper layers to reduce computational cost. This results in approximately 235 million cells in the domain.

There are two steps in the simulations. The first step is the precursor simulation in which the turbulent ABLs are generated. A periodic boundary condition is applied to all lateral boundaries for an empty flow domain where the horizontal driving pressure gradient is adjusted every time step to control the mean wind speed and direction at the hub height (Churchfield et al., 2012). This is done by determining the source term from the error between the actual planar-averaged velocity at the specified height and the desired velocity. This approach is suitable for turbine engineering analyzes in which the hub height wind speed can be prescribed. However, it is acknowledged that this method cannot simultaneously achieve both the desired geostrophic wind vector and the hub height wind direction. The Schumann wall shear stress model is used for wall modeling at the bottom surface, while the top boundary is a free-slip wall. The precursor simulation is performed until the turbulent flow reaches quasi-steady state before the flow data on a cross flow plane are recorded to be used as the inflow for the wind farm simulations.

The second step is the wind farm simulation, in which the stream-wise boundaries are changed to inlet and outlet boundary conditions, respectively. The bottom and top boundaries are identical to the precursor simulation. The turbines are modeled using an actuator disk method with a simple controller in which the rotor speed and pitch angle are functions of the average axial velocity across the rotor (Troldborg and Andersen, 2023). The aerodynamic forces and power of the rotors are calculated using the blade element method. A simple yaw controller is implemented to keep the rotor facing local wind directions. The statistical calculations for the turbulent flow and turbine output are performed over the last hour of the simulation time after the initial pass.

3 Results

The numerical results from different numerical solvers are compared in the following subsections. The results include inflow conditions, wind farm flows, wind farm performance, and wind farm efficiency.

3.1 Inflow Profiles

As mentioned in Section 2, each participant uses different approaches to obtain atmospheric flows. Figures 2- 4 illustrate the vertical inflow profiles generated by the different solvers, where u and v are velocity components in the streamwise and spanwise directions, respectively, M corresponds the magnitude of horizontal wind velocity vectors, Φ denotes the wind angle between the wind vector and the x-axis, Θ is potential temperature and e corresponds to the turbulent kinetic energy (TKE).

In general, all solvers produce similar inflow profiles near the rotor height. The velocity profile of the H150 case exhibits a low-level jet-like shape where the peak of supergeostrophic wind speeds is observed close to 200 m height. Wind veering is also significant in the H150 case where the wind direction difference between the top and bottom of the rotor is almost 15°, while it is less than 5° in the H500 and H500-dh500 cases.

It should be noted that UU may not achieve the geostrophic wind speed of 10 m/s because the mean wind speed and direction are controlled at the hub height as presented in Section 2.5. Furthermore, it was challenging to achieve quasi-steady state for UU due to the initial oscillation of the wind speeds above the capping inversion. The main deviations considering veer, potential temperature and turbulence kinetic energy is in figure 2(f) where the SOWFA setup differs due to lack of ability to resolve the smallest scales due to the required numerical cost. However, this problem does not affect the results in figure 3(f), where the deeper boundary layer has less wind shear. There are no significant differences for the velocities and tke profiles between the H500 and H500-dh500 cases; only the potential temperature profile differs due to the initial capping inversion thickness (Figures 3 and 4).

Another notable outlier is the DNV potential temperature profile for the H150 case. As can be seen in figure 2(e), the inversion in the DNV profile is thicker and starts at a lower height compared with the other simulations. The precursor simulations for all the models started from the same potential temperature profile, with the inversion starting at 150 m and a ground potential temperature of 288.15 K, but the DNV precursor approach preserves the initial potential temperature profile to a greater degree than the other approaches, resulting in material differences in the conditions at the simulated wind farms. DNV created a second set of inflow profiles from a precursor simulating using a potential temperature profile more consistent with the inflow profiles from the other four contributors; this second set of H150 profiles (not shown) is much more similar to the other profiles, particularly the wind speed and wind direction profiles.

3.2 Wind Farm Flows

The mean streamwise velocity, averaged across the wind farm width at hub height, is presented in Figure 5 from 25D upstream to 65D downstream of the first row turbines. Overall, all solvers indicate a more significant decrease in the wind speed in the H150 case compared to the H500 and H500-dh500 cases. To quantify and compare wake recovery, mean wind speeds are

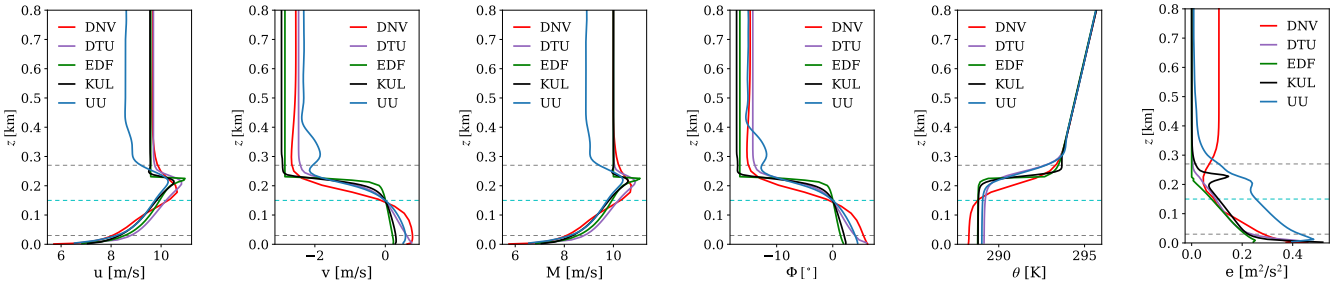

(a) Velocity, u (b) Velocity, v (c) $\sqrt{u^2+v^2}$ (d) $\arctan(\frac{v}{u})$ (e) Temperature (f) TKE

Figure 2. Inflow profiles of the H150 case.

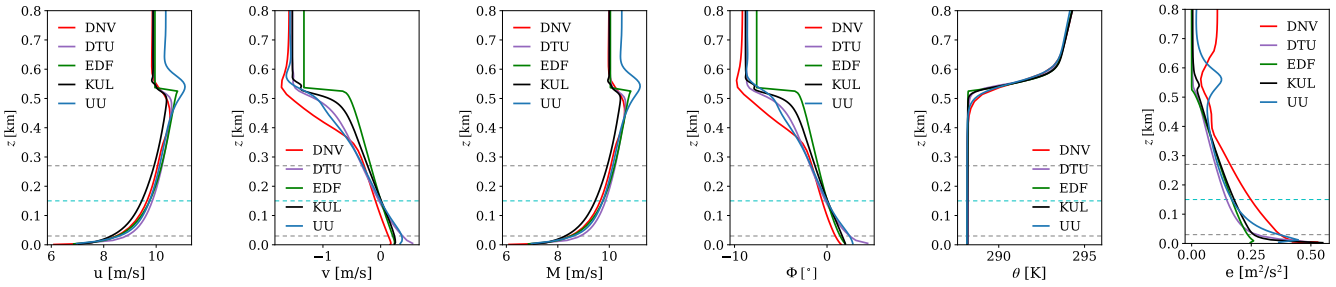

(a) Velocity, u (b) Velocity, v (c) $\sqrt{u^2+v^2}$ (d) $\arctan(\frac{v}{u})$ (e) Temperature (f) TKE

Figure 3. Inflow profiles of the H500 case.

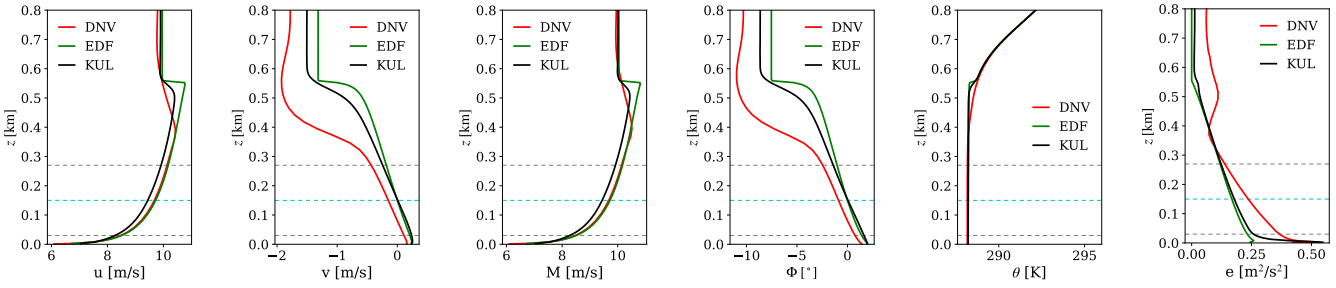

(a) Velocity, u (b) Velocity, v (c) $\sqrt{u^2+v^2}$ (d) $\arctan(\frac{v}{u})$ (e) Temperature (f) TKE

Figure 4. Inflow profiles of the H500-dh500 case.

normalized by the wind speed 25D upstream of the wind farm, as shown in Figure 6. For the H150 case, EDF, KUL, DTU and UU predict a similar wake recovery rate, with the velocity reductions of approximately 30-40% relative to the free-stream winds, while DNV estimates a reduction over 40%. For the H500 case, UU overpredict wake recovery compared to EDF, KUL and DNV, while DTU switches between following the trend of UU and the other models. The H500-dh500 case shows similar

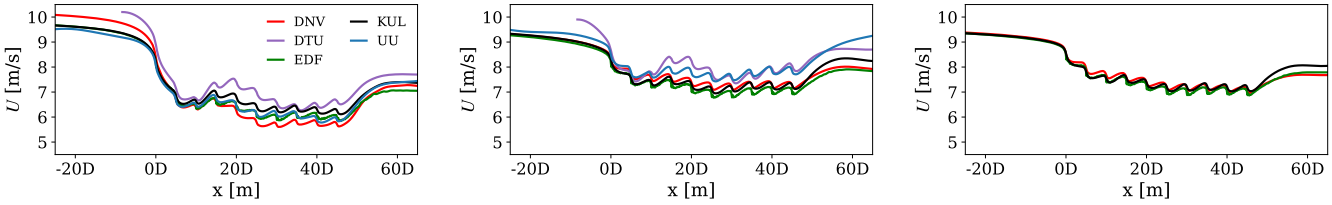

(a) H150 (b) H500 (c) H500-dh500

Figure 5. Mean streamwise velocity averaged over the wind farm width at the hub height.

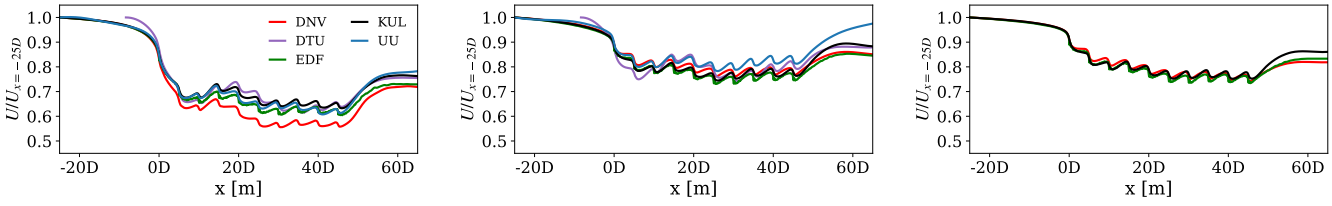

(a) H150 (b) H500 (c) H500-dh500

Figure 6. Normalised mean streamwise velocity averaged over the wind farm width at the hub height.

trends to the H500 case and thus suggests that the capping inversion thickness does not significantly affect the wind farm wake flows.

Figures 7 - 9 show the stream-wise velocity contours for the H150, H500, and H500-dh500 cases, respectively, in a xy plane at hub height. In the H150 case (Figure 7), the shallow boundary layer restricts the flow above the wind farm and this leads to a stronger deflection of the wakes at the edges of the farm compared to the 500 m BLH cases shown in Figures 8 and 9.

The stronger wind veering in the shallow boundary layer results in more pronounced skewed wakes, as illustrated in a cross-flow (yz) plane 10D downstream of the last row turbines (Figures 10, 11 and 12).

Further wind speed comparisons on the xz and yz planes can be found in Appendix B.

3.3 Wind Farm Performance

The performance of the wind farm is quantified and compared using power output and turbine yaw angle. Figures 13 - 15 illustrate the row-averaged power output for each case including absolute power output, power normalized by the first row (P/P_1), and power normalized by an isolated turbine output (P/P_∞). It is noted that the isolated turbine output data for all solvers can be found in Appendix A. For the H150 case, all solvers give a similar row-averaged power output trend where the power reduces approximately by almost 20% in the second row. For instance, the P/P_∞ of the second rows (Figures 13c, 14c and 15c) are approximately 60% for the H150 case and more than 70% for the H500 and H500-dh500 cases. Even though this is a staggered layout wind farm where the second row is not directly in the wake of the first row, this significant power

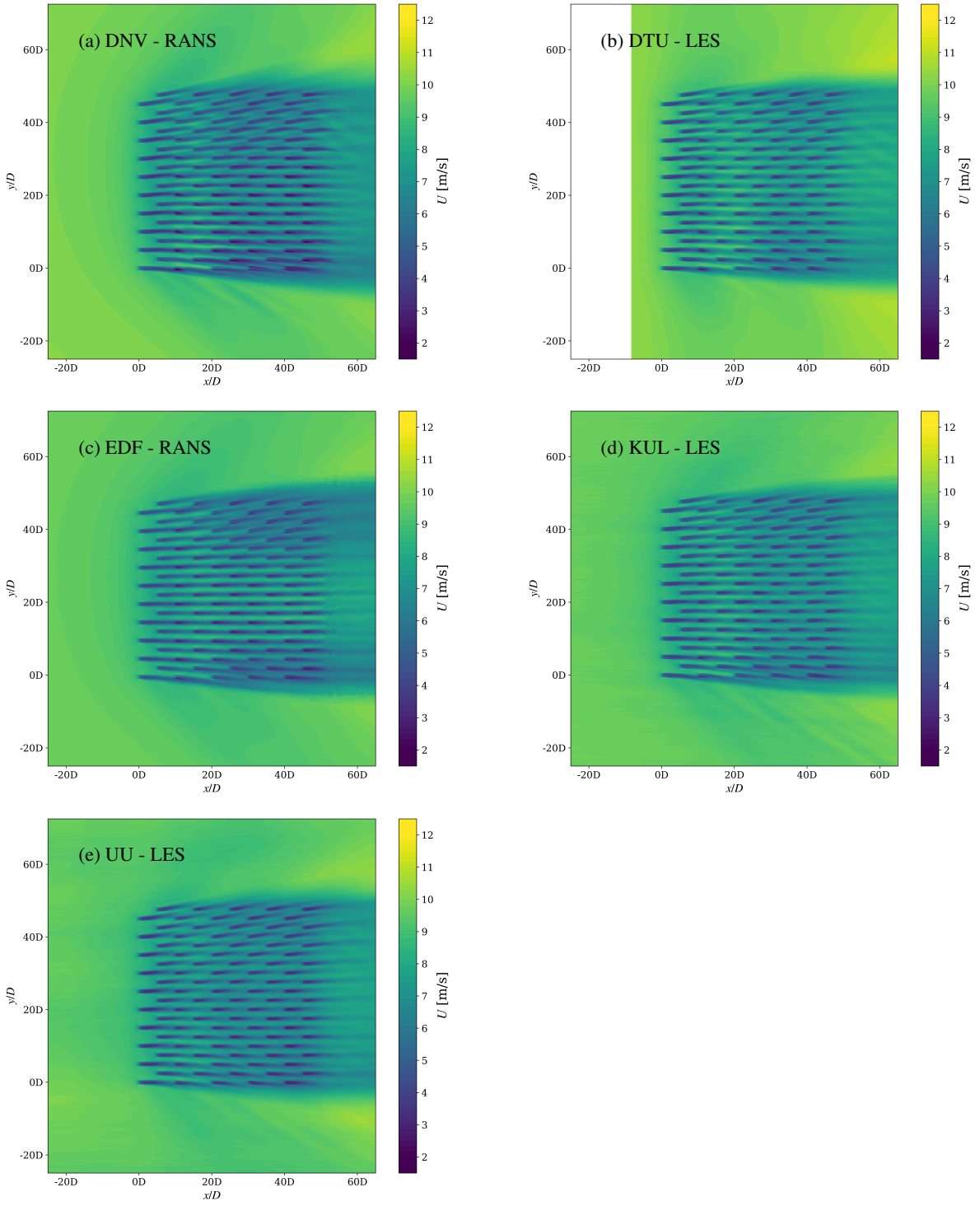

Figure 7. Mean streamwise velocity on the XY plane at hub height for the H150 case.

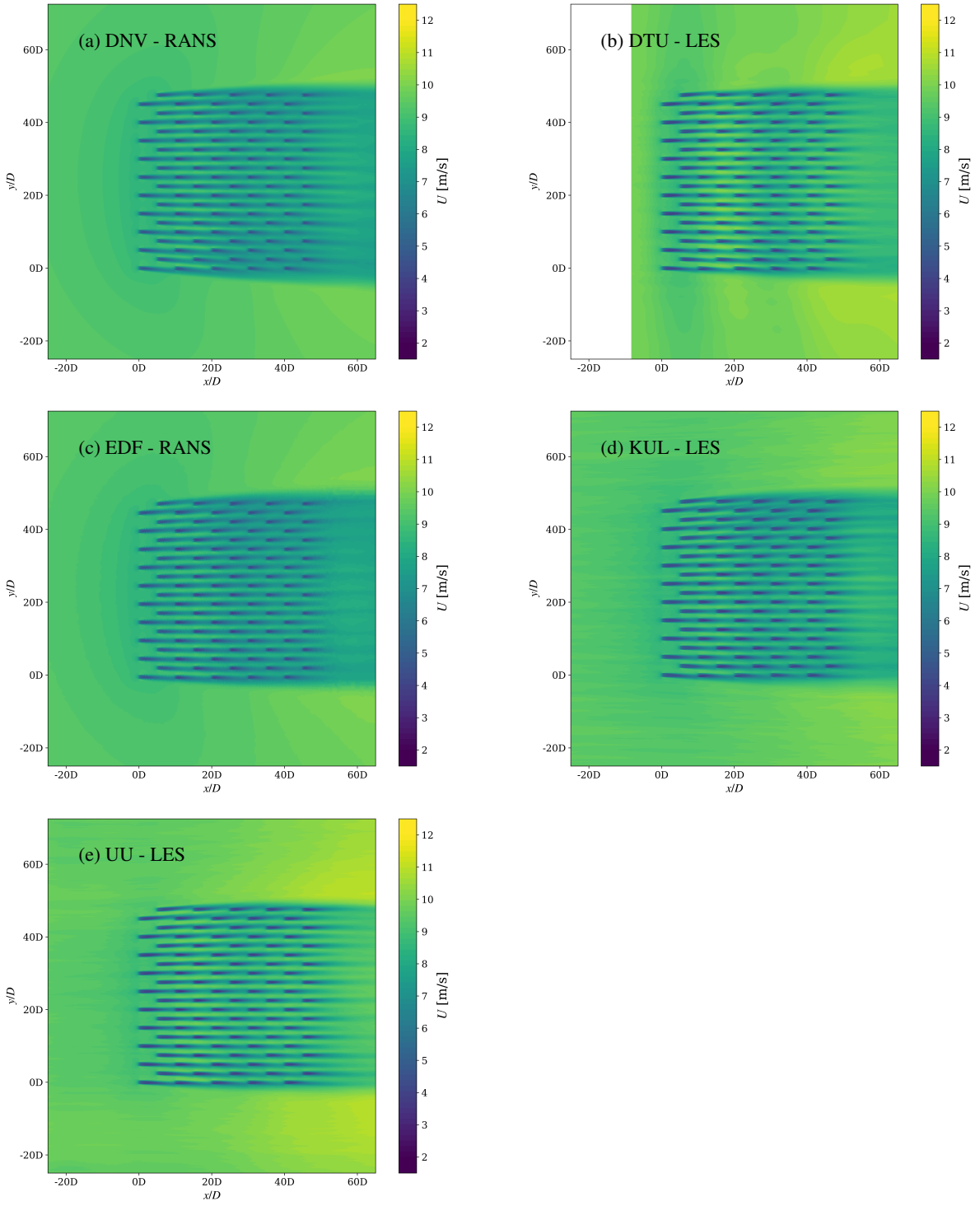

Figure 8. Mean streamwise velocity on the XY plane at hub height for the H500 case.

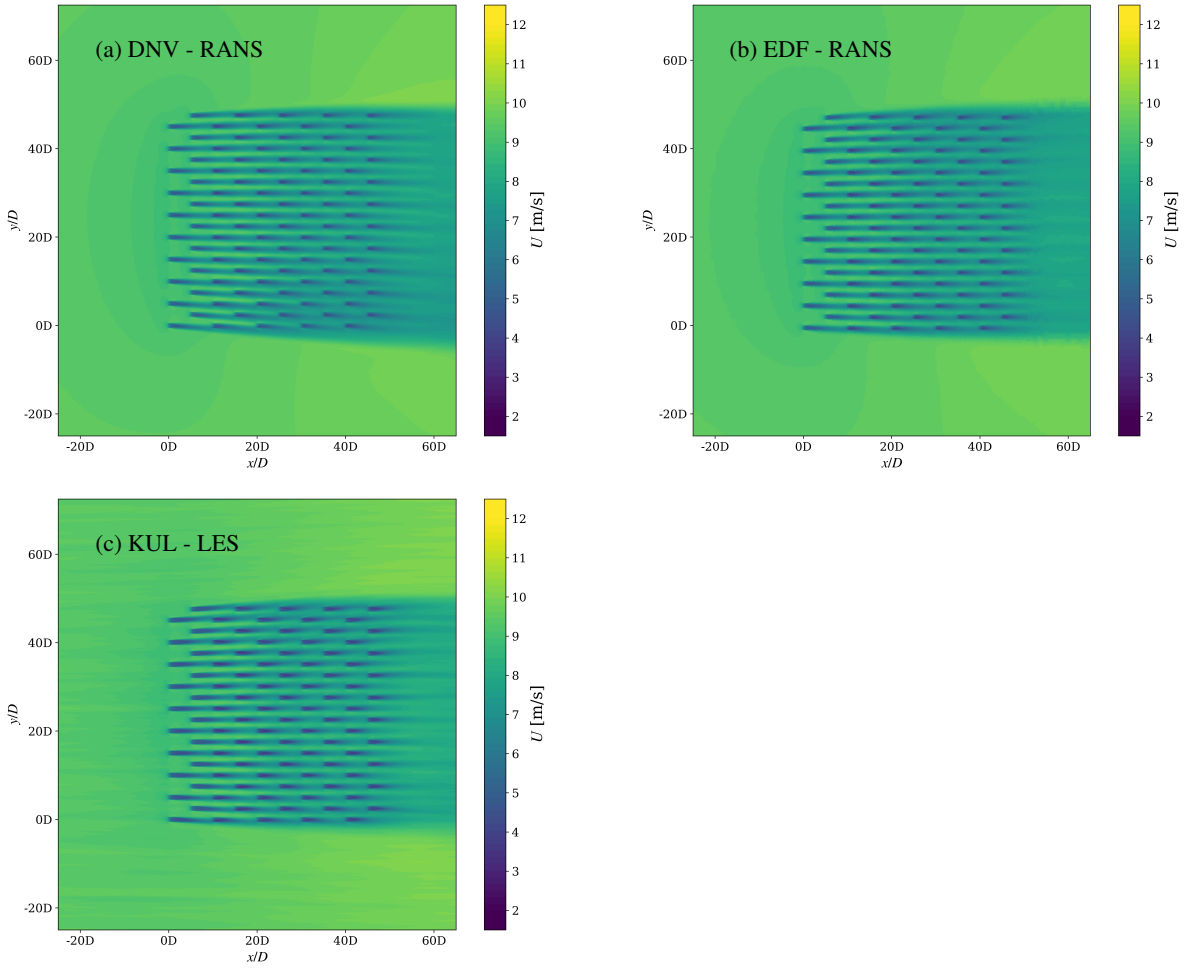

Figure 9. Mean streamwise velocity on the XY plane at hub height for the H500-dh500 case.

reduction in the second row indicates a strong blockage effect in the H150 case compared to the other cases. The power drops further in the third row before it recovers in the fourth and fifth rows. Since DTU and UU did not simulate the H500-dh500 case, fewer results are available for comparison, which makes the results in Figure 15 appear less distinct than those in Figures 13 and 14.

In Figure 16, the power distribution in the farm is depicted. The left, middle and right columns represent the H150, H500 and H500-dh-500 cases, respectively. In all cases, the turbines near the edges of the front rows generate more power than the turbines in the middle.

The averaged turbine yaw angles are presented in Figure 17. Each turbine in the farm responds to the local wind direction by yawing the rotor to maximize the power output. For the H150 case, the more pronounced spanwise flows cause the turbines close to sides of the farm to yaw more significantly where the averaged yaw angles are more than 10°.

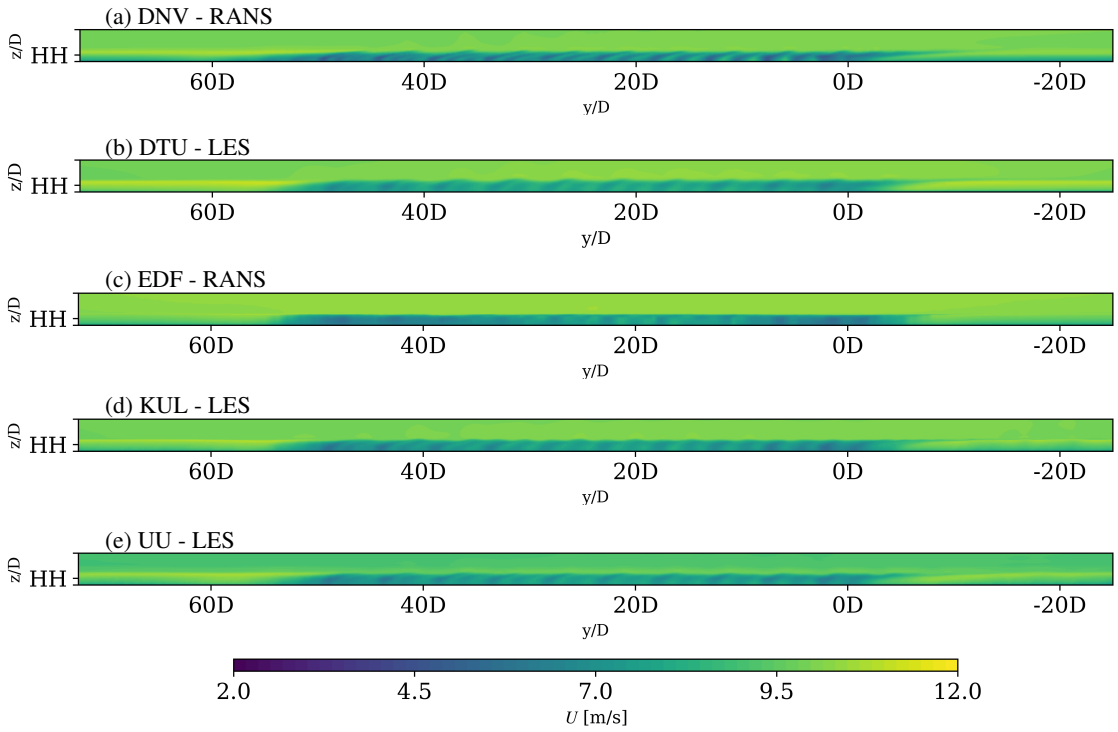

Figure 10. Mean streamwise velocity on the YZ plane 10D downstream of the last row for the H150 case, viewing downstream.

3.4 Wind Farm Efficiencies

Wind farm power production losses due to blockage and wake interactions are quantified by the following definitions as introduced by Allaerts and Meyers (2018b). Losses due to wake interactions or wake efficiency (η_w) can be expressed as:

$$\eta_w = \frac{P_{\text{tot}}}{N\,P_1}, \tag{1}$$

where P_{tot} describes the total wind farm power output, N number of turbines in a farm and P_1 is the power of front-row turbines. The losses due to non-local effects, i.e. the blockage effect can be expressed as:

$$\eta_{nl} = \frac{P_1}{P_\infty}, \tag{2}$$

where P_∞ is obtained from single turbine simulations. The total wind farm efficiency (η_{farm}) is then the product of losses introduced by non-local and wake effects,

$$\eta_{\text{farm}} = \eta_w\,\eta_{nl}. \tag{3}$$

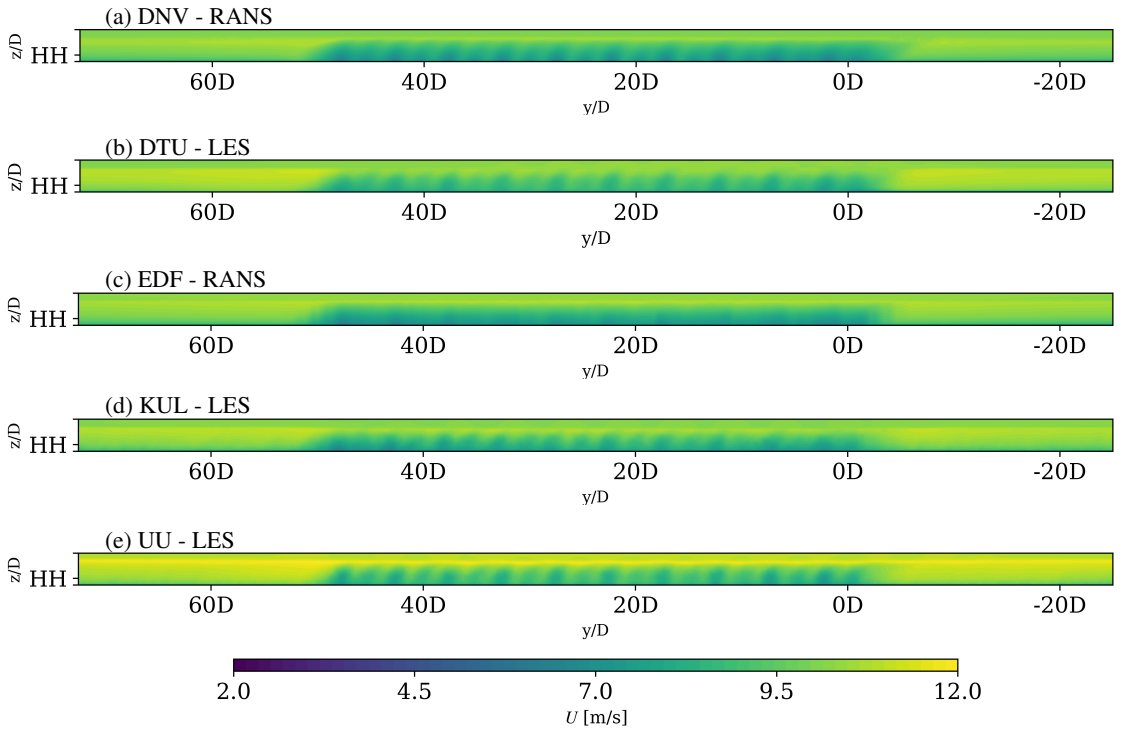

Figure 11. Mean streamwise velocity on the YZ plane 10D downstream of the last row for the H500 case, viewing downstream.

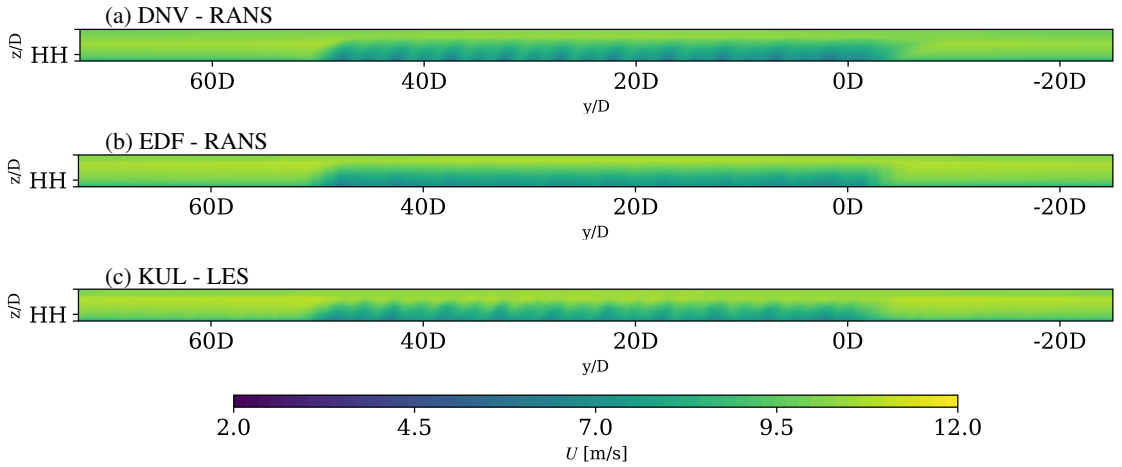

Figure 12. Mean streamwise velocity on the YZ plane 10D downstream of the last row for the H500-dh500 case, viewing downstream.

The efficiencies calculated from Equations 1, 2 and 3 are summarized in Table 3, 4 and 5. The results indicate that wind farm efficiency is highly dependent on the depth of the boundary layer. In the H150 case, losses from wake interaction can reach

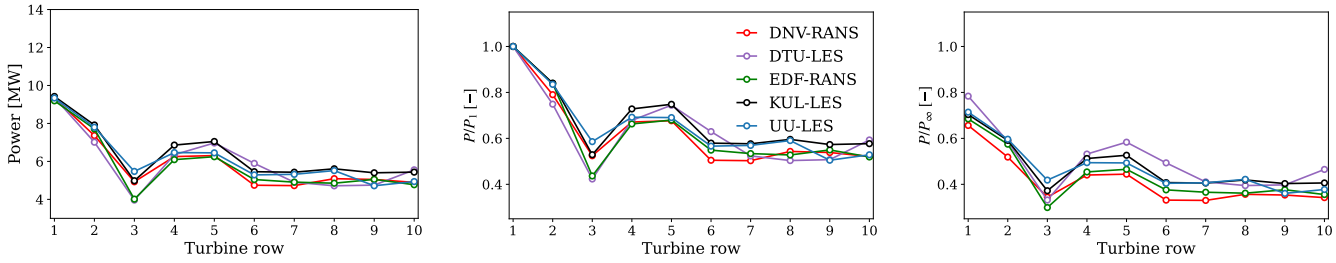

(a) (b) (c)

Figure 13. Row-averaged power output for the H150 case: (a) absolute power output, (b) power output normalized by the first row, and (c) power output normalized by an isolated turbine power.

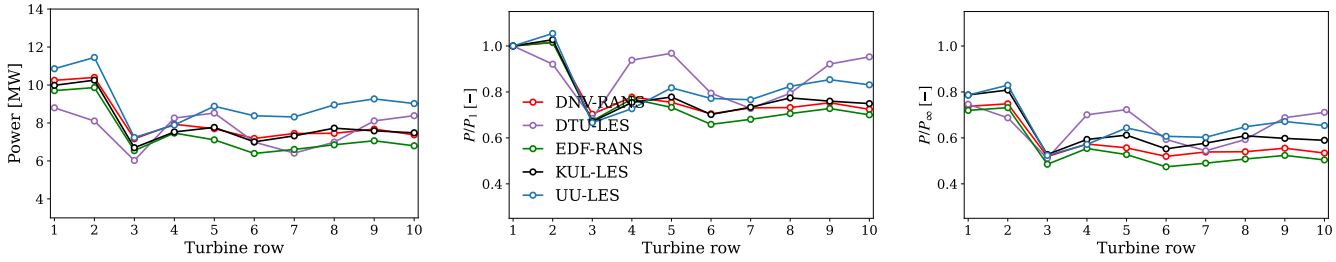

(a) (b) (c)

Figure 14. Row-averaged power output for the H500 case: (a) absolute power output, (b) power output normalized by the first row, and (c) power output normalized by an isolated turbine power.

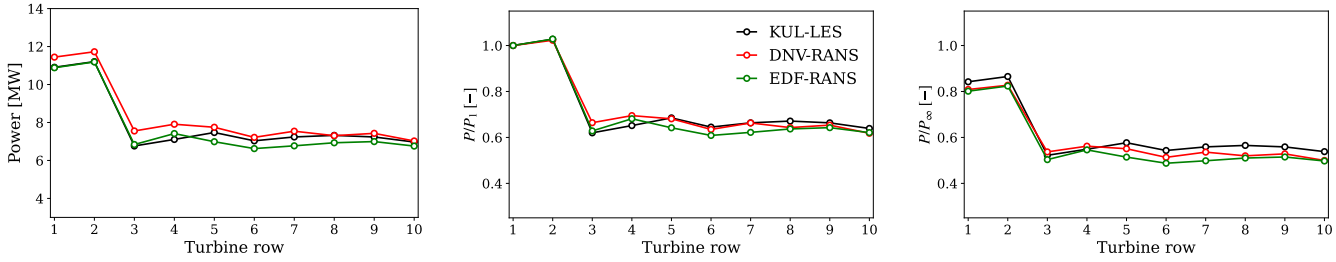

(a) (b) (c)

Figure 15. Row-averaged power output for the H500-dh500 case: (a) absolute power output, (b) power output normalized by the first row, and (c) power output normalized by an isolated turbine power.

nearly 40%, while in the H500 case, they are around 20%. Furthermore, due to the blockage effect, the front-row turbines can generate approximately 70% and 80% of the output of an isolated turbine in shallow and deeper boundary layers, respectively.

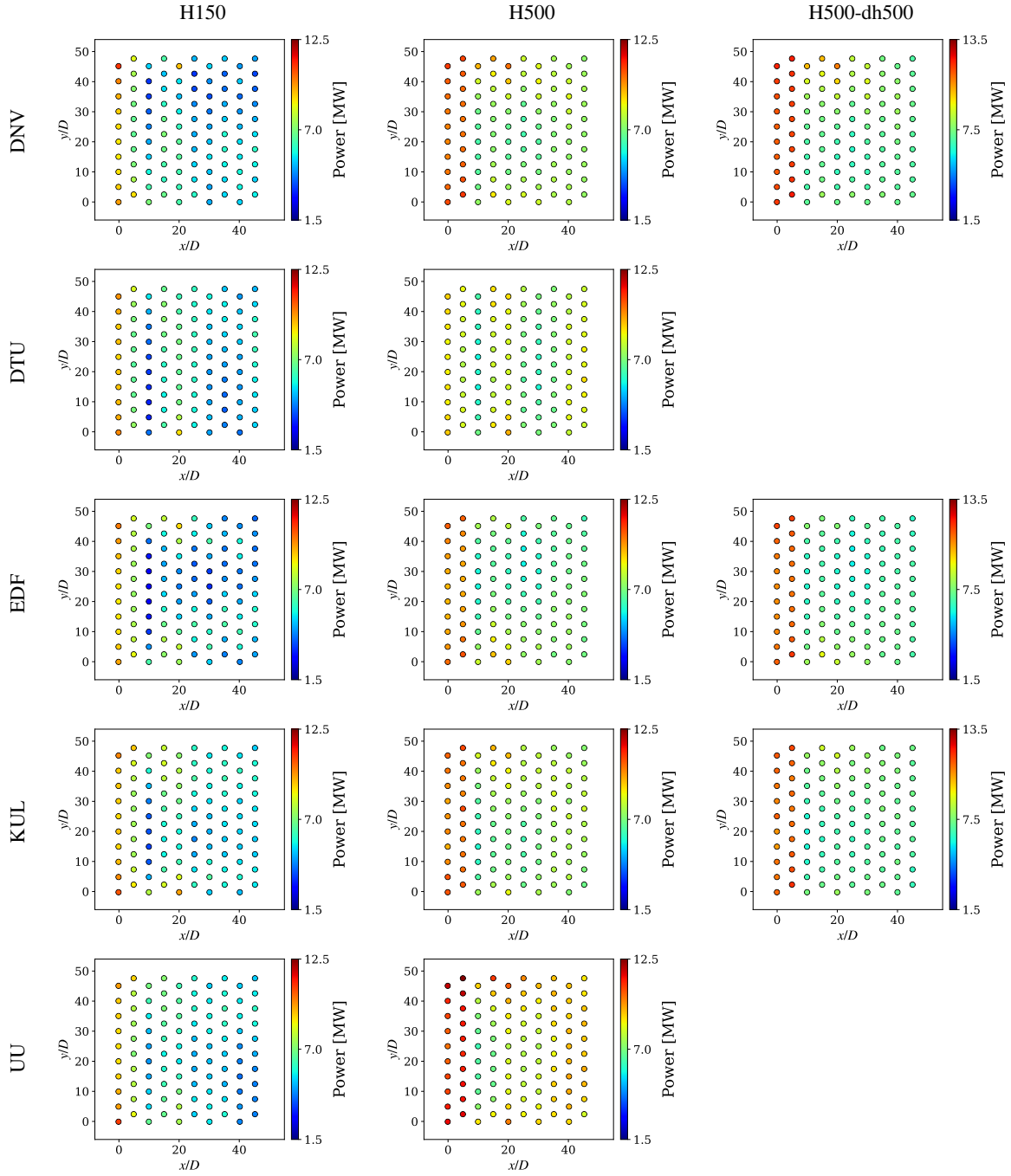

Figure 16. The power distribution in the farm is depicted.

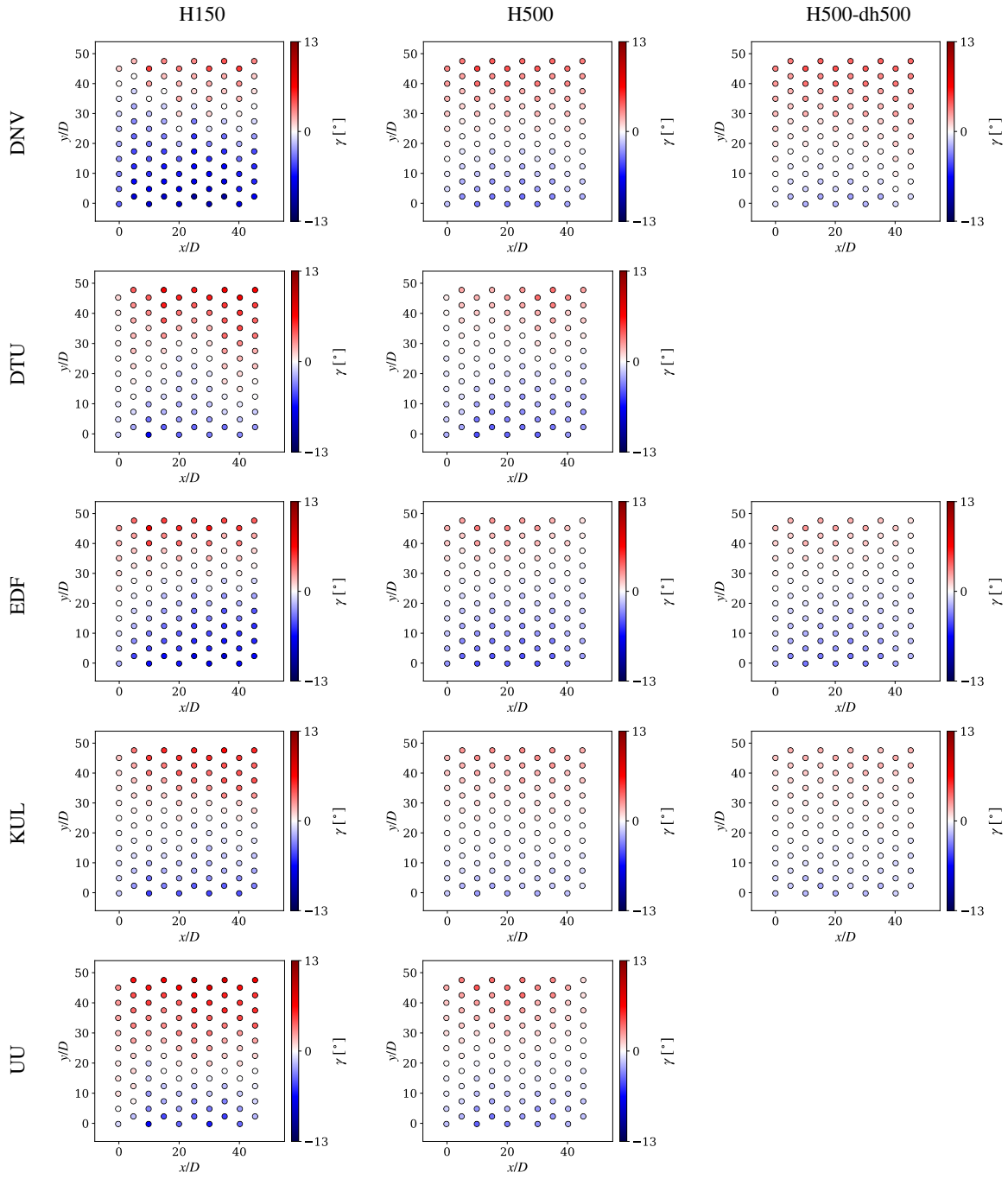

Figure 17. Local wind direction.

The efficiencies also reveal the influence of capping inversion thickness on wind farm performance. Results from DNV, EDF and KUL show that the case with a thicker capping inversion leads to a reduced blockage effect but slightly larger wake losses compared to the thinner capping inversion.

The DNV H150 results are an outlier relative to the other models, with lower relative wind speeds through the wind farm (Figure 6(a)) and lower wind farm efficiency (Table 3). The gap between the DNV wind farm calculation and the others for this case is simply a consequence of simulating a different potential temperature profile, which corresponds to a thinner boundary layer. When the DNV H150 case is rerun with inflow profiles more consistent with those of the other contributors, the wind speeds through the farm (not shown) and the calculated efficiencies (η_{nl}= 0.695, η_{w} = 0.620, and η_{farm}= 0.431) are more like the results from the others. The level of agreement is similar to how the DNV results compare with other results for the H500 and H500-dh500 cases. Thus, the outlier wind farm predictions from DNV presented for the H150 case has more to do with inflow conditions than differences between the models.

We here would like to highlight that the level of non-local blockage depends on the simulated conditions and selected dense wind farm layout. In this case, the power density is approximately 12 MW/km^2. This is in the range of the Belgium offshore economic zone and the German Bight but denser compared to Danish and UK offshore cases.

In addition, the calculated efficiencies are a lot lower than would be calculated in an energy yield analysis, which would involve simulations over a much broader range of conditions, include wind directions and wind speeds where the efficiencies are at or very close to 1.0. However, our focus is not on the overall AEP calculations, but rather on the quality and comparison of codes to represent wind farm flows under strong blockage conditions.

Table 3. Wind Farm Efficiencies for the H150 Case

	η_{nl}	η_{w}	η_{f}
KUL	0.704	0.675	0.475
DNV	0.656	0.627	0.412
EDF	0.685	0.630	0.431
UU	0.714	0.656	0.469
DTU	0.784	0.635	0.498

Table 4. Wind Farm Effiecies for the H500 Case

	η_{nl}	η_{w}	η_{f}
KUL	0.787	0.795	0.625
DNV	0.737	0.790	0.582
EDF	0.720	0.767	0.552
UU	0.786	0.831	0.654
DTU	0.747	0.870	0.650

Table 5. Wind Farm Efficiencies for the H500-dh500 Case

	η_{nl}	η_{w}	η_{f}
KUL	0.842	0.727	0.612
DNV	0.809	0.728	0.588
EDF	0.801	0.711	0.570

4 Discussion

Based on the results presented in Section 3, there are a few issues that need to be discussed further. Firstly, there are discrepancies in the inflow profiles generated by different numerical approaches because the simulations were set up according to the best practice of each solver to match the specified atmospheric conditions. The geostrophic winds generated by UU do not match other solvers at 10 m/s due to the wind speed and direction control approach. UU also overestimated the TKE for the H150 case due to the relatively coarse mesh resolution in the LES precursor. However, key features, including wind shear, wind veer, and potential temperature, are comparable. It should be noted that the aim of this study was not to provide a code-to-code comparison to verify flow solvers. In order to conduct a proper code comparison, reference inflow conditions, i.e., met mast or LiDAR data, should be available for validation (Doubrawa et al., 2020; Asmuth et al., 2022). Instead, the purpose of this study is to illustrate the impact of the BLH and capping inversion thickness on a large wind farm operation using various numerical approaches. The results of different fidelity models, stretching from RANS to LES, show convincing trends in the wind farm performance and highlight the importance of the BLH.

Another source of difference between the simulation tools is the turbine representation, as described in Section 2. The turbine-induced aerodynamic forces differ, as KUL and EDF used a non-rotating disk model, while DNV, DTU and UU used a rotating disk model. It is difficult to isolate the impact of this discrepancy in the current set of simulations, as other factors, such as differences in inflow conditions and mesh resolutions, are also involved. Some previous studies have demonstrated that the choice between non-rotating and rotating disk methods may only affect the near-wake profile, while both models yield good agreement in the far wake (Meyers and Meneveau, 2010; Wu and Porté-Agel, 2011; van der Laan et al., 2015). However, the impact of turbine-induced force distribution on wind farm efficiency, particularly a dense wind farm, has yet to be verified. Furthermore, the turbine controllers also differ among the tools: EDF and KUL used a constant thrust coefficient, DNV and UU used an averaged disk velocity to reference tabulated data, and DTU simulated a full controller within an aeroelastic code. These differences cause the turbines to respond differently to the incoming flows. For instance, DTU's full controller is capable of simulating a more realistic turbine response under varying wind shear and wind veer in the H150 and H500 cases, as the variable speed and pitch are controlled using the instantaneous torque on the disks as the input signal. However, the simpler controllers used by DNV and UU may underestimate the impact of varying velocity shear and directional veer on the turbine power output due to the averaging of rotor disk velocity. This issue is particularly significant for the large rotor size of the 15 MW turbine, as it can cause the turbines to respond differently to the incoming flows, and using a static or dynamic controller

can significantly impact the estimated power production (Troldborg and Andersen, 2023). Nevertheless, although it is important to acknowledge these differences in turbine models, we would like to emphasize that the single turbine simulations that were used to normalize results (e.g. in terms of non-local and wake efficiency) partly factor out these differences.

Secondly, simulations of a large wind farm require a sufficiently large computational domain to minimize wind farm blockage, as demonstrated by Lanzilao and Meyers (2024). The height of the domain is suggested to be more than 20 km (Allaerts and Meyers, 2017; Lanzilao and Meyers, 2024) to prevent reflection waves being trapped near the inlet, and to be able to resolve wind farm-induced gravity waves. However, due to limitations in computational resources and demand using an LES approach, it was challenging for UU to simulate such a large domain extent with OpenFOAM CFD software. UU uses a domain height of 6 km with a 3 km thick Rayleigh damping layer at the top boundary, while DNV, EDF and KUL utilize 25 km domain height, resulting in reflection waves trapped near the inlet for both BLH cases that were not completely eliminated, as illustrated in Figure 18. These non-physical waves affect wind farm flows, and improved numerical solutions are needed to mitigate wave reflections in large wind farm simulations with an inflow-outflow boundary condition approach (Khan et al., 2024; Stipa et al., 2024). DTU is for the same reason as UU using a limited domain height. Despite a 3 km domain height, DTU do not identify reflection waves. This is probably due to a large Reyleigh damping, but further investigations are required.

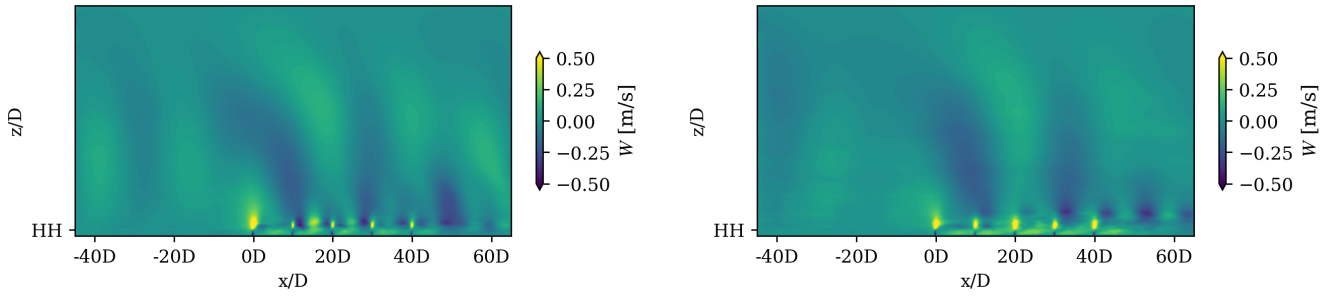

(a) H150

(b) H500

Figure 18. Time-averaged vertical velocity contour from UU SOWFA on the xz plane through the sixth turbine column. The axes are normalized by rotor diameter, D, with $0D$ on the x-axis indicating the location of the first-row turbines.

Thirdly, to examine the influence of BLH on wind farm operations, a neutral ABL with varying capping inversion heights was employed to minimize the influencing factors. However, BLH is governed by atmospheric stability and surface conditions, which can lead to considerable variations in atmospheric turbulence. Low BLHs are generally associated with a stably stratified ABL characterized by weaker turbulence, whereas an unstable ABL tends to have enhanced vertical mixing. Consequently, the findings of this study do not fully capture the complexities of BLH's impact. Variations in turbulence levels across different BLHs may influence wake recovery within and behind a wind farm, thereby affecting overall performance.

In this study, different levels of modeling fidelity have been used with different numerical approaches. The overall results show good agreement. However, one cannot conclude that the results of farm efficiency are independent of the fidelity level. In this study, we do not investigate details on momentum entrainment. where one could expect the different fidelity levels to show

differences. However, when assessing the overall efficiency under these specific conditions using the best practice in setup, etc. The different fidelity models agree well considering trends but with quantitative differences.

Lastly, while all solvers in this comparison exhibit overall similar trends on wind farm performance and efficiency in various BLH scenarios, there is a lack of field observations to validate these large wind farm simulation results. We would also like to clarify here that the levels of efficiency presented here correspond to a few specific cases with an undisturbed wind speed close to the rated, a relatively dense farm, and one wind direction aligned with the staggered layout. Therefore, the level of efficiency presented here for these cases should not be considered to be a general efficiency of a wind farm. To make that assessment, one needs to run a large set of simulations and weight them to climatology at specific sites.

5 Conclusions

This study investigates the impact of atmospheric boundary layer (ABL) height on the performance of gigawatt-scale wind farms. Through numerical simulations using multiple CFD solvers, the effects of ABL height and capping inversion on wind farm power generation, efficiency, and flow dynamics were analyzed.

The results indicate that a lower ABL height (for example, 150 m) leads to greater blockage and wake interaction effects, that is, reduced farm efficiency and higher energy losses compared to deeper boundary layers (for example, 500 m). Furthermore, the thickness of the capping inversion layer was found to influence the wake recovery behind the wind farm.

The numerical simulations conducted by various research institutions and industry partners showed consistent overall trends, though significant variations were observed depending on the computational methods and domain size. The simulation cases performed are complex, and the results of the different methods show a variation of up to 10 $\%$ and further research is needed to limit this gap. Based on these results, it is not clear to what extent the variation depends on the fidelity level of the models used.

In summary, the study confirms that a deeper ABL generally improves the efficiency of wind farms and reduces energy losses due to blockage effects. The findings emphasize the importance of incorporating the height and stability of the ABL in wind energy models to improve the accuracy of the power generation predictions.

Code and data availability. The flow fields and turbine outputs for all codes can be provided upon request.

Appendix A: Single Turbine Simulation Output

Table A1. H150

	P [MW]	U_{d} [m/s]	γ [$^\circ$]
KUL	13.38	6.95	-0.12
DNV	14.36	7.31	0.80
EDF	13.42	6.88	0.62
UU	13.08	7.40	-1.62
DTU	11.95	8.38	-0.83

Table A2. H500

	P [MW]	U_{d} [m/s]	γ [$^\circ$]
KUL	12.68	6.83	-0.08
DNV	13.98	7.25	0.48
EDF	13.48	6.89	-0.01
UU	13.80	7.55	0.15
DTU	11.78	8.42	-1.06

Table A3. H500-dh500

	P [MW]	U_{d} [m/s]	γ [$^\circ$]
KUL	12.95	6.88	-0.06
DNV	14.23	7.29	0.90
EDF	13.58	6.91	0.05

Appendix B: Wind Farm Flows on xz and yz Planes

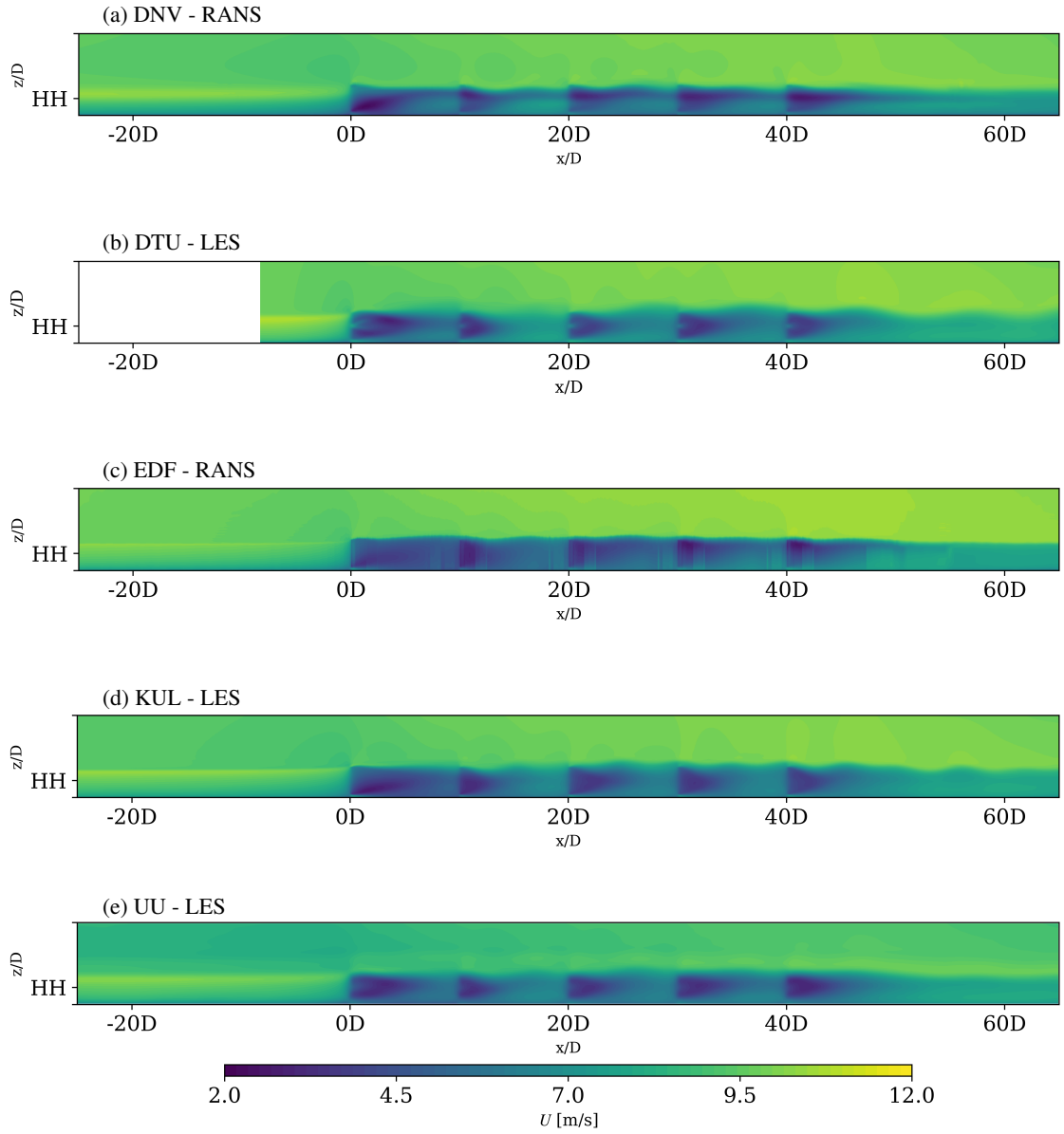

Figure B1. Mean streamwise velocity on the XZ plane at the sixth column turbines for the H150 case.

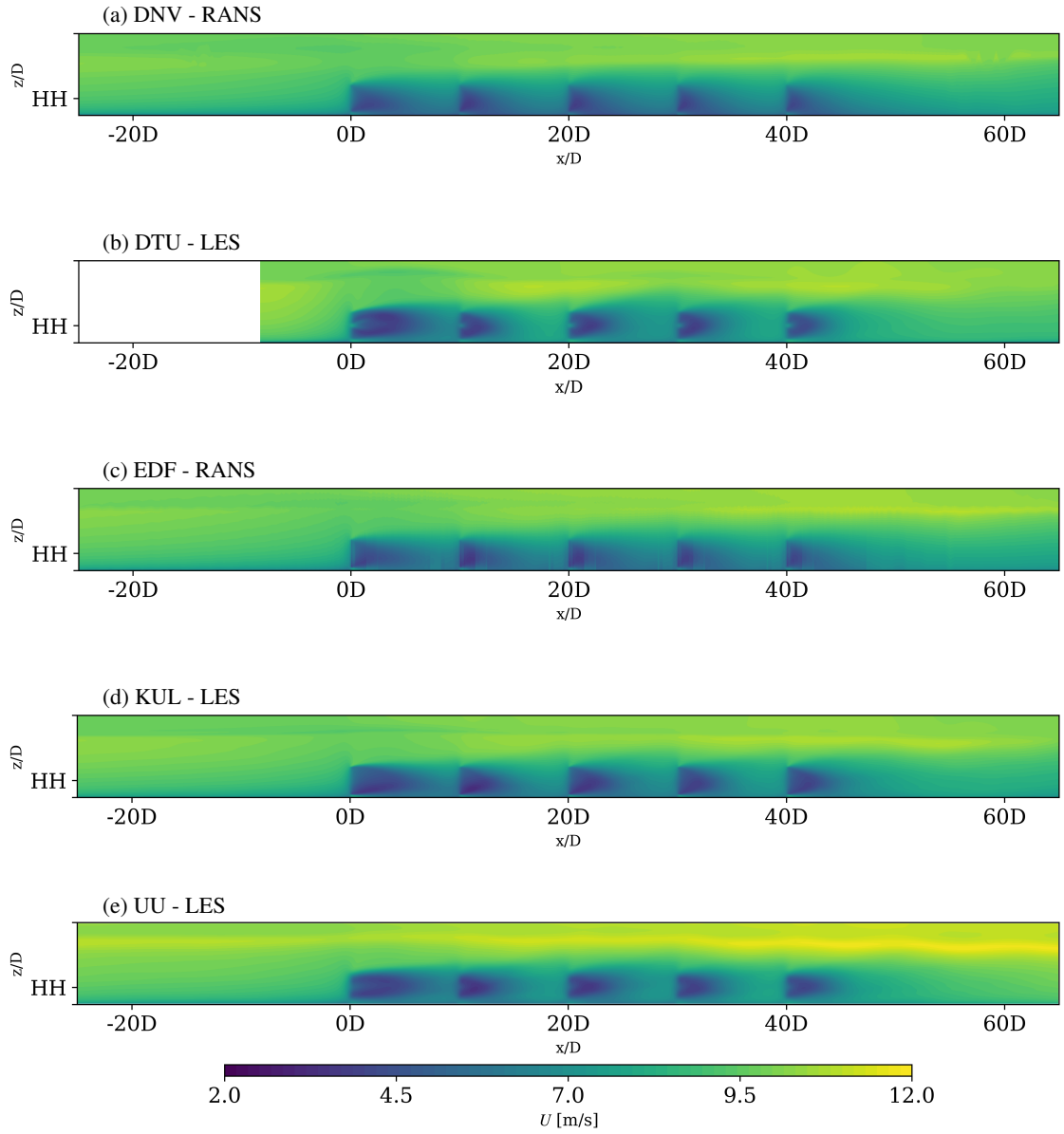

Figure B2. Mean streamwise velocity on the XZ plane at the sixth column turbines for the H500 case.

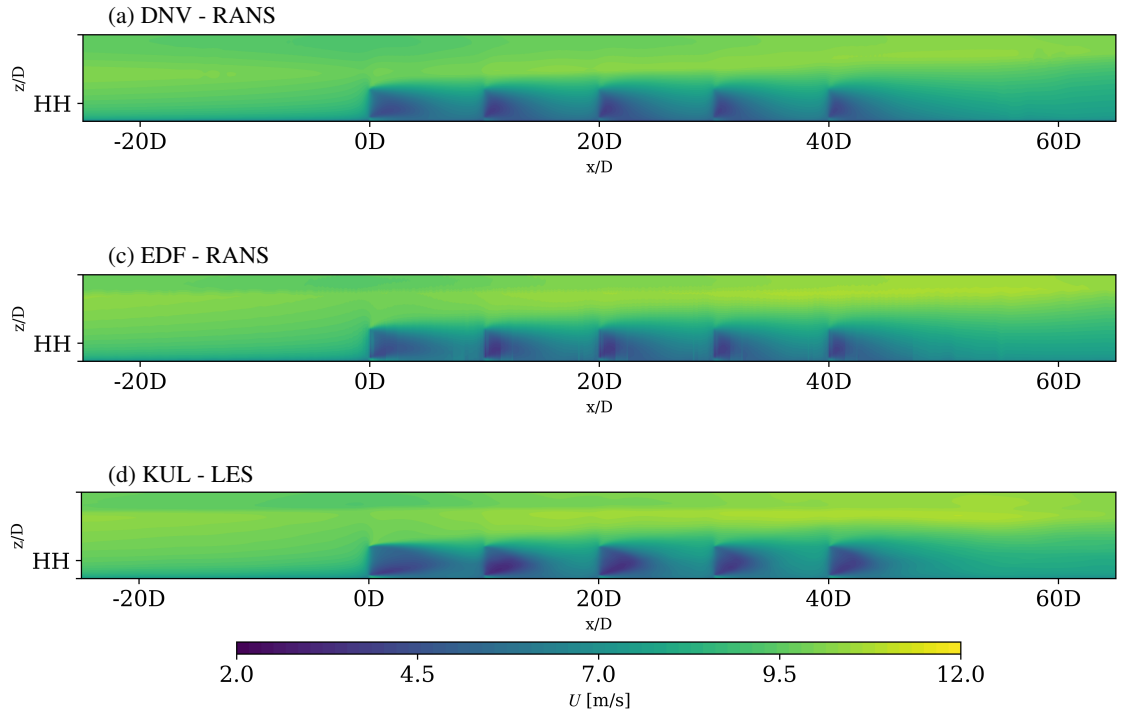

Figure B3. Mean streamwise velocity on the XZ plane at the sixth column turbines for the H500-dh500 case.

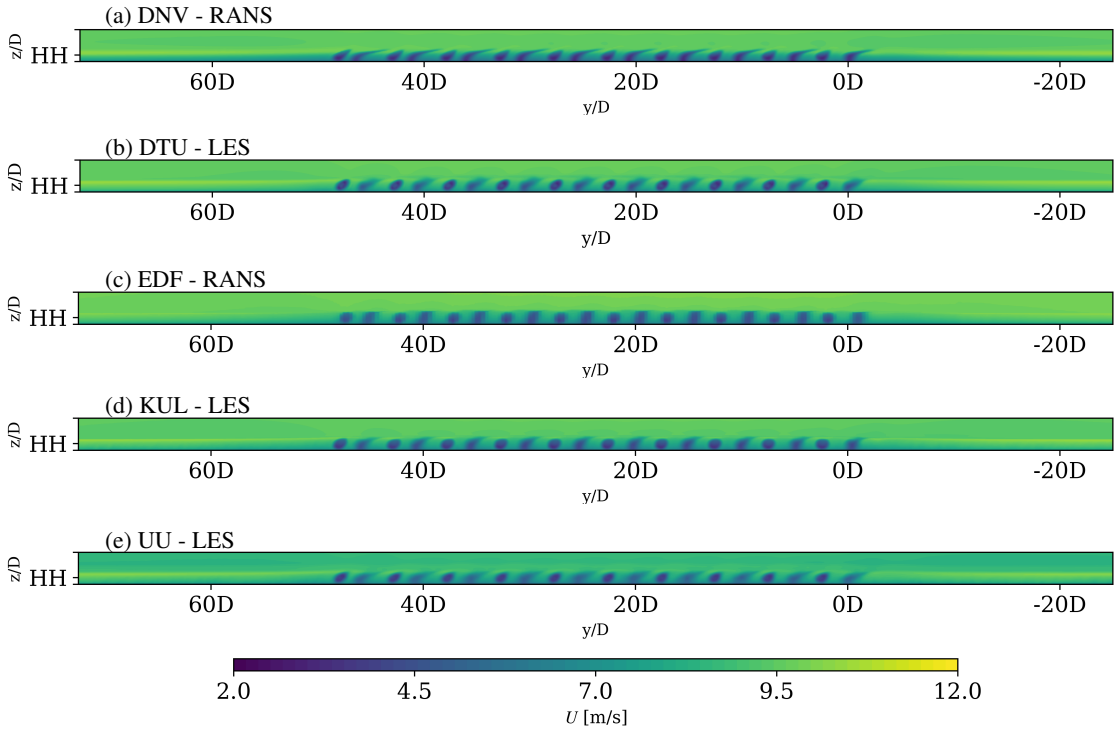

Figure B4. Mean streamwise velocity on the YZ plane 7.5D downstream of the first row for the H150 case, viewing downstream.

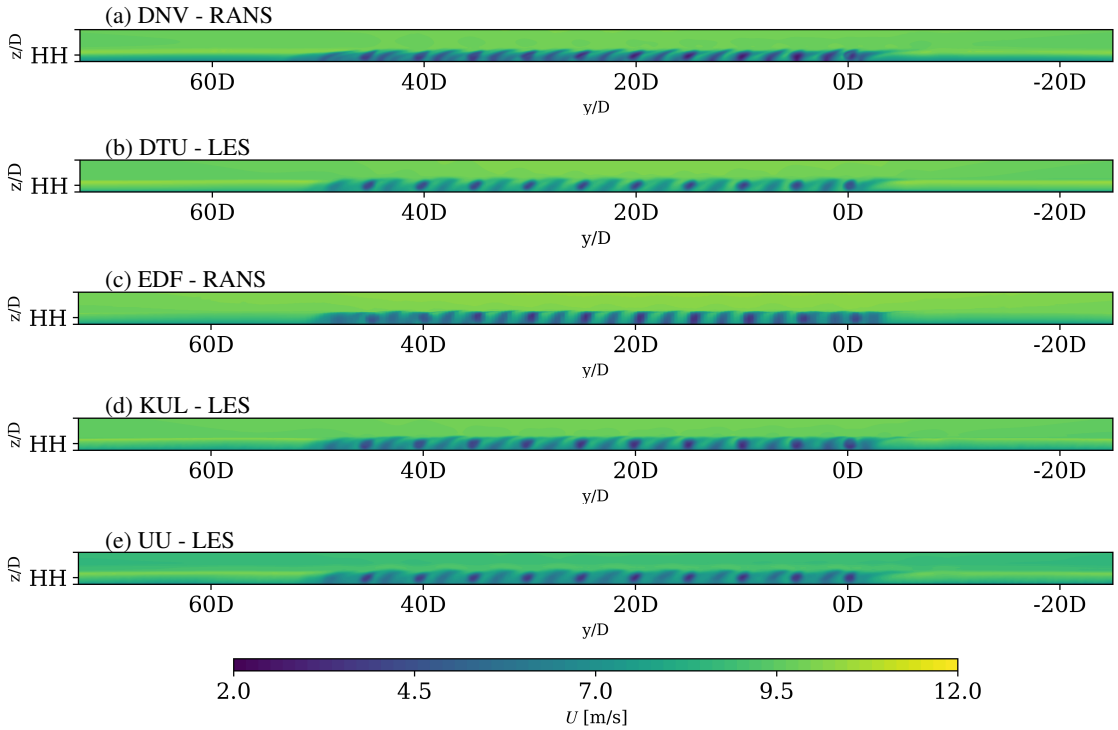

Figure B5. Mean streamwise velocity on the YZ plane 22.5D downstream of the first row for the H150 case, viewing downstream.

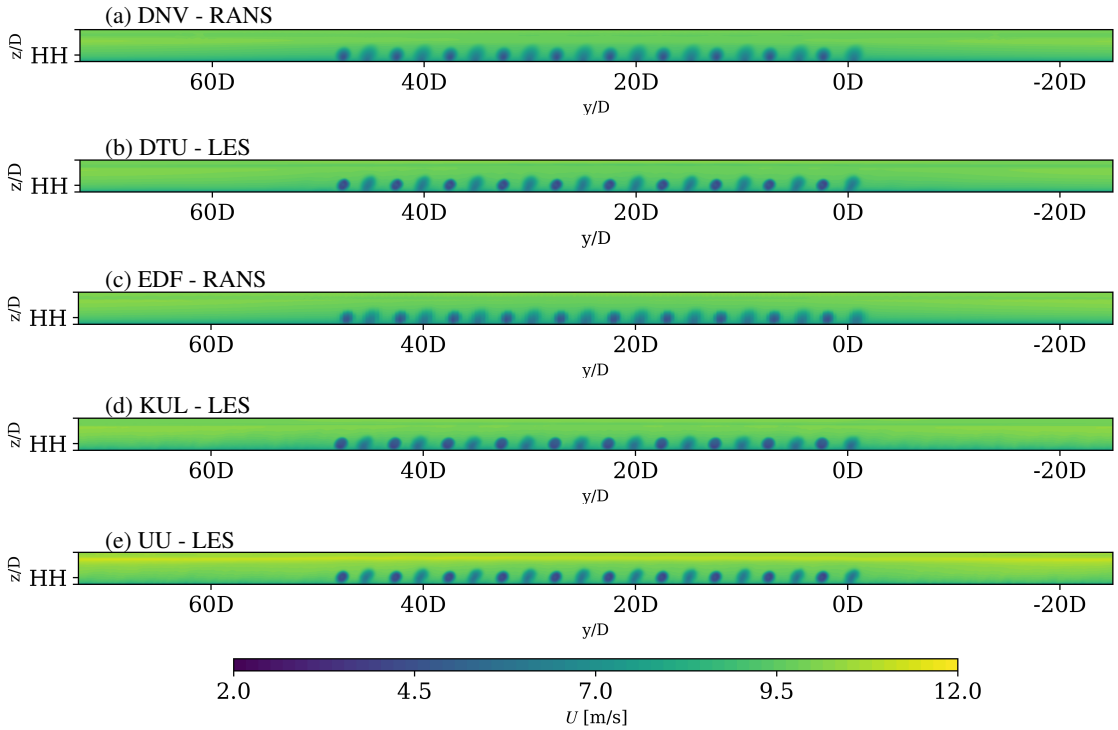

Figure B6. Mean streamwise velocity on the YZ plane 7.5D downstream of the first row for the H500 case, viewing downstream.

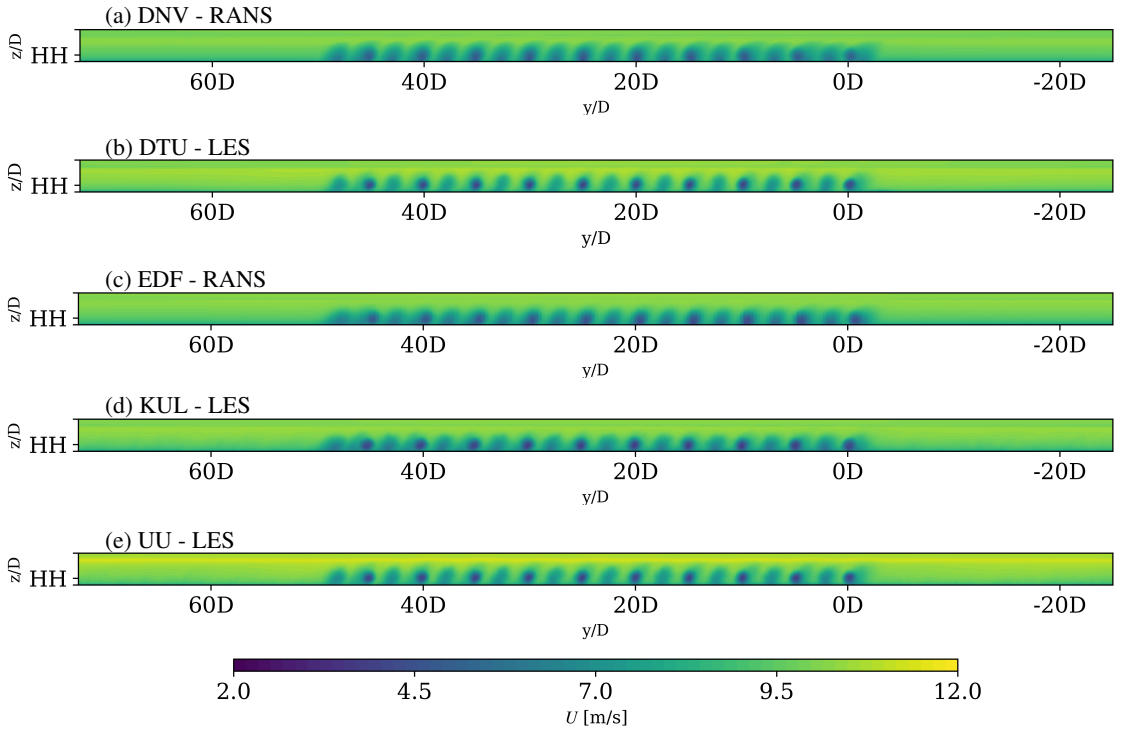

Figure B7. Mean streamwise velocity on the YZ plane 22.5D downstream of the first row for the H500 case, viewing downstream.

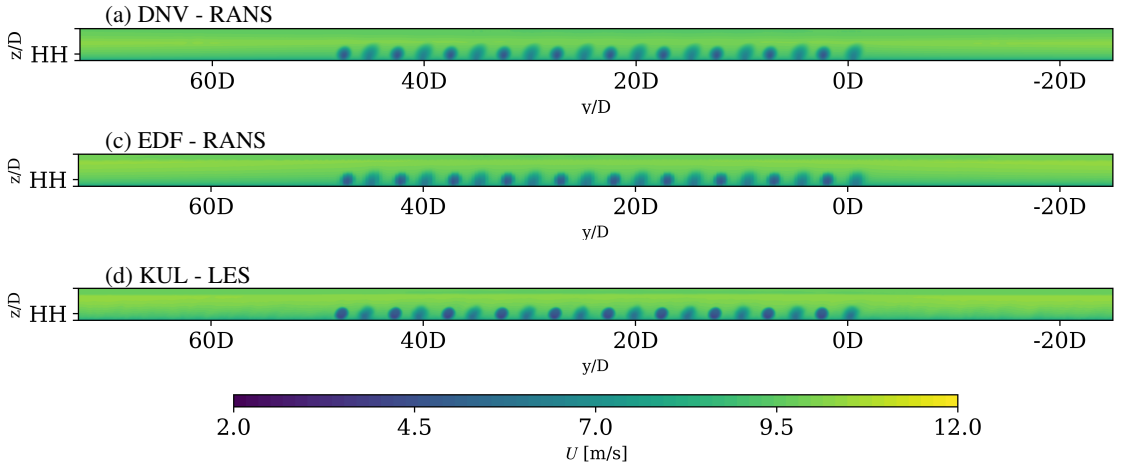

Figure B8. Mean streamwise velocity on the YZ plane 7.5D downstream of the first row for the H500-dh500 case, viewing downstream.

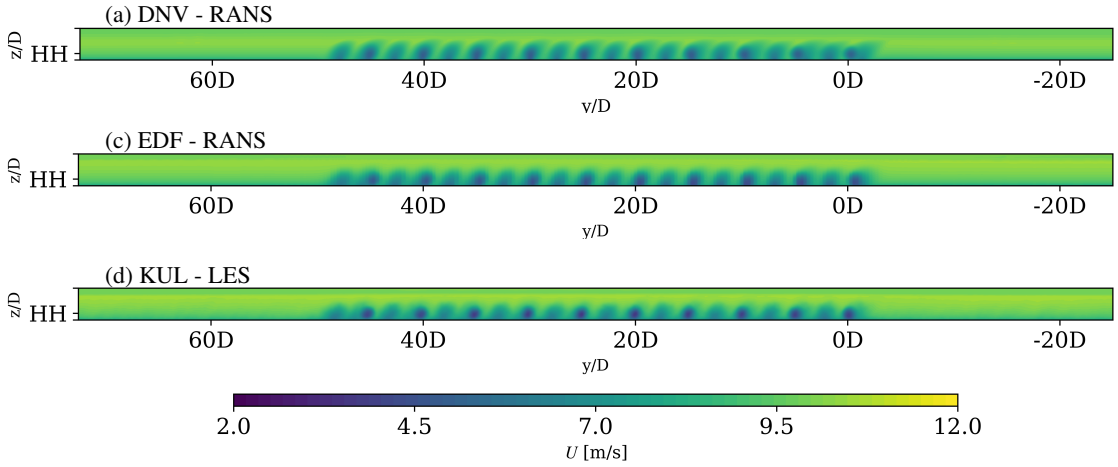

Figure B9. Mean streamwise velocity on the YZ plane 22.5D downstream of the first row for the H500-dh500 case, viewing downstream.

Author contributions. SI coordinated the development of the article. WC and LL gathered and postprocessed the data. WC, LL, JB, AM, RSM, NT, and SJA performed simulations with input and supervision from coauthors. ED provided input to the code_saturne simulations. HOE provided input to the OpenFOAM simulations. The manuscript was mainly written by SI, WC, JM, JB, and AM and reviewed by all.

Competing interests. The authors declare that they have no conflict of interest.

Acknowledgements. This work has been funded by the FLOW project (Atmospheric Flow, Load and pOwer for Wind energy) within the EU H2020 programme (grant no. 101084205). The simulations were performed using resources provided by Swedish National Infrastructure for Computing (SNIC) and the National Academic Infrastructure for Supercomputing in Sweden (NAISS).

References

Abkar, M., Bae, H. J., and Moin, P.: Minimum-dissipation scalar transport model for large-eddy simulation of turbulent flows, Phys. Rev. Fluids, 1, 041 701, https://doi.org/10.1103/PhysRevFluids.1.041701, 2016.

Allaerts, D.: Large-eddy simulation of wind farms in conventionally neutral and stable atmospheric boundary layers, Ph.D. thesis, KULeuven, Leuven, Belgium, 2016.

Allaerts, D. and Meyers, J.: Large eddy simulation of a large wind-turbine array in a conventionally neutral atmospheric boundary layer, Physics of Fluids, 27, 065 108, https://doi.org/10.1063/1.4922339, 2015.

Allaerts, D. and Meyers, J.: Boundary-layer development and gravity waves in conventionally neutral wind farms, J. Fluid Mech., 814, 95–130, 2017.

Allaerts, D. and Meyers, J.: Gravity Waves and Wind-Farm Efficiency in Neutral and Stable Conditions, Boundary-Layer Meteorol., 166, 269–299, 2018a.

Allaerts, D. and Meyers, J.: Gravity waves and wind-farm efficiency in neutral and stable conditions, Boundary-layer meteorology, 166, 269–299, 2018b.

Asmuth, H., Navarro Diaz, G. P., Madsen, H. A., Branlard, E., Meyer Forsting, A. R., Nilsson, K., Jonkman, J., and Ivanell, S.: Wind turbine response in waked inflow: A modelling benchmark against full-scale measurements, Renewable Energy, 191, 868–887, https://doi.org/https://doi.org/10.1016/j.renene.2022.04.047, 2022.

Bleeg, J. and Montavon, C.: Blockage effects in a single row of wind turbines, Journal of Physics: Conference Series, 2265, 022 001, https://doi.org/10.1088/1742-6596/2265/2/022001, 2022.

Bleeg, J., Purcell, M., Ruisi, R., and Traiger, E.: Wind Farm Blockage and the Consequences of Neglecting Its Impact on Energy Production, Energies, 11, https://doi.org/10.3390/en11061609, 2018.

Calaf, M., Meneveau, C., and Meyers, J.: Large eddy simulation study of fully developed wind-turbine array boundary layers, Phys. Fluids, 22, 015 110, https://doi.org/10.1063/1.3291077, 2010.

Canuto, C., Hussaini, M. Y., Quarteroni, A., and Zang, T. A.: Spectral Methods in Fluid Dynamics, Springer-Verlag, Berlin, Germany, doi:10.1007/978-3-642-84108-8, 1988.

Churchfield, M. J., Lee, S., Michalakes, J., and Moriarty, P. J.: A numerical study of the effects of atmospheric and wake turbulence on wind turbine dynamics, Journal of Turbulence, 13, N14, https://doi.org/10.1080/14685248.2012.668191, 2012.

Deardorff, J. W.: Stratocumulus-capped mixed layers derived from a three-dimensional model, Boundary-layer meteorology, 18, 495–527, 1980.

Delport, S.: Optimal control of a turbulent mixing layer, Ph.D. thesis, KULeuven, Leuven, Belgium, 2010.

Doubrawa, P., Quon, E. W., Martinez-Tossas, L. A., Shaler, K., Debnath, M., Hamilton, N., Herges, T. G., Maniaci, D., Kelley, C. L., Hsieh, A. S., Blaylock, M. L., van der Laan, P., Andersen, S. J., Krueger, S., Cathelain, M., Schlez, W., Jonkman, J., Branlard, E., Steinfeld, G., Schmidt, S., Blondel, F., Lukassen, L. J., and Moriarty, P.: Multimodel validation of single wakes in neutral and stratified atmospheric conditions, Wind Energy, 23, 2027–2055, https://doi.org/https://doi.org/10.1002/we.2543, 2020.

Fornberg, B.: A Practical Guide to Pseudospectral Methods, Cambridge Monographs on Applied and Computational Mathematics, Cambridge University Press, https://doi.org/10.1017/CBO9780511626357, 1996.

Gaertner, E., Rinker, J., Sethuraman, L., Zahle, F., Anderson, B., Barter, G., Abbas, N., Meng, F., Bortolotti, P., Skrzypinski, W., Scott, G., Feil, R., Bredmose, H., Dykes, K., Sheilds, M., Allen, C., and Viselli, A.: Definition of the IEA 15-Megawatt Offshore Reference Wind Turbine, Tech. rep., International Energy Agency, https://www.nrel.gov/docs/fy20osti/75698.pdf, 2020.

Guimet, V. and Laurence, D.: A linearised turbulent production in the k-ε model for engineering applications, Proceedings of the 5th International Symposium on Engineering Turbulence Modelling and Measurements, pp. 157–166, 2002.

Hodgson, E. L., Grinderslev, C., Meyer Forsting, A. R., Troldborg, N., Sørensen, N. N., Sørensen, J. N., and Andersen, S. J.: Validation of Aeroelastic Actuator Line for Wind Turbine Modelling in Complex Flows, Frontiers in Energy Research, 10, 1–20, 2022.

Hodgson, E. L., Souaiby, M., Troldborg, N., Porté-Agel, F., and Andersen, S. J.: Cross-code verification of non-neutral ABL and single wind turbine wake modelling in LES, J. Phys. Conf. Ser., 2505, 012 009, 2023.

Khan, M. A., Watson, S. J., Allaerts, D. J. N., and Churchfield, M.: Recommendations on setup in simulating atmospheric gravity waves under conventionally neutral boundary layer conditions, Journal of Physics: Conference Series, 2767, 092 042, https://doi.org/10.1088/1742-6596/2767/9/092042, 2024.

Klemp, J. B. and Lilly, D. K.: Numerical simulations of hydrostatic mountain waves, Journal of the atmospheric sciences, 35, 78–107, https://doi.org/10.1175/1520-0469(1978)035<0078:NSOHMW>2.0.CO;2, 1977.

Lanzilao, L. and Meyers, J.: Effects of self-induced gravity waves on finite wind-farm operations using a large-eddy simulation framework, Journal of Physics: Conference Series, 2265, 022 043, https://doi.org/10.1088/1742-6596/2265/2/022043, 2022.

Lanzilao, L. and Meyers, J.: An Improved Fringe-Region Technique for the Representation of Gravity Waves in Large Eddy Simulation with Application to Wind Farms, Boundary-Layer Meteorology, https://doi.org/10.1007/s10546-022-00772-z, 2023.

Lanzilao, L. and Meyers, J.: A parametric large-eddy simulation study of wind-farm blockage and gravity waves in conventionally neutral boundary layers, Journal of Fluid Mechanics, 979, A54, https://doi.org/10.1017/jfm.2023.1088, 2024.

Larsen, T. J. and Hansen, A. M.: How 2 HAWC2, the user's manual, 2007.

Mason, P. J. and Thomson, D. J.: Stochastic backscatter in large-eddy simulations of boundary layers, Journal of Fluid Mechanics, 242, 51–78, https://doi.org/10.1017/S0022112092002271, 1992.

Meyer Forsting, A. R., Navarro Diaz, G. P., Segalini, A., Andersen, S. J., and Ivanell, S.: On the accuracy of predicting wind-farm blockage, Renewable Energy, 214, 114–129, https://doi.org/https://doi.org/10.1016/j.renene.2023.05.129, 2023.

Meyers, J. and Meneveau, C.: Large eddy simulations of large wind-turbine arrays in the atmospheric boundary layer, in: 48th AIAA aerospace sciences meeting including the new horizons forum and aerospace exposition, p. 827, 2010.

Meyers, J. and Sagaut, P.: Is plane-channel flow a friendly case for the testing of large-eddy simulation subgrid-scale models?, Physics of Fluids, 19, https://doi.org/10.1063/1.2722422, 048105, 2007.

Michelsen: Basis 3D—A Platform for Development of Multiblock PDE Solvers, Tech. rep., Danmarks Tekniske Universitet, 1992.

Michelsen, J. A.: Block structured Multigrid solution of 2D and 3D elliptic PDE's, Tech. Rep. Technical University of Denmark AFM 94-06, 1994.

Mikkelsen, R.: Actuator Disc Methods Applied to Wind Turbines, Ph.D. thesis, 2004.

Porté-Agel, F., Bastankhah, M., and Shamsoddin, S.: Wind-turbine and wind-farm flows: a review, Boundary-layer meteorology, 174, 1–59, 2020.

Rampanelli, G. and Zardi, D.: A Method to Determine the Capping Inversion of the Convective Boundary Layer, Journal of Applied Meteorology, 43, 925 – 933, https://doi.org/10.1175/1520-0450(2004)043<0925:AMTDTC>2.0.CO;2, 2004.

Sanchez Gomez, M., Lundquist, J. K., Mirocha, J. D., and Arthur, R. S.: Investigating the physical mechanisms that modify wind plant blockage in stable boundary layers, Wind Energy Science Discussions, 2023, 1–28, https://doi.org/10.5194/wes-2023-20, 2023.

Sescu, A. and Meneveau, C.: A control algorithm for statistically stationary large-eddy simulations of thermally stratified boundary layers: A Control Algorithm for LES of Thermally Stratified Boundary Layers, Quarterly Journal of the Royal Meteorological Society, 140, 2017–2022, https://doi.org/10.1002/qj.2266, 2014.

Shen, W. Z., Michelsen, J. A., Sørensen, N. N., and Nørkær Sørensen, J.: An improved SIMPLEC method on collocated grids for steady and unsteady flow computations, Numerical Heat Transfer: Part B: Fundamentals, 43, 221–239, 2003.

Smith, R. B.: Gravity wave effects on wind farm efficiency, Wind Energy, 13, 449–458, https://doi.org/10.1002/we.366, 2010.

Sørensen, J. N., Mikkelsen, R. F., Henningson, D. S., Ivanell, S., Sarmast, S., and Andersen, S. J.: Simulation of wind turbine wakes using the actuator line technique, Phil. Trans. R. Soc. A, 373, 20140 071, 2015.

Sørensen, N. N.: General Purpose Flow Solver Applied to Flow over Hills, Ph.D. thesis, Technical University of Denmark, 1995.

Stevens, B., Moeng, C. H., and Sullivan, P. P.: Entrainment and subgrid length scales in large-eddy simulations of atmospheric boundary-layer flows, Symposium on Developments in Geophysical Turbulence, 58, 253–269, 2000.

Stipa, S., Ahmed Khan, M., Allaerts, D., and Brinkerhoff, J.: A large-eddy simulation (LES) model for wind-farm-induced atmospheric gravity wave effects inside conventionally neutral boundary layers, Wind Energy Science, 9, 1647–1668, https://doi.org/10.5194/wes-9-1647-2024, 2024.

Stull, R. B.: An Introduction to Boundary Layer Meteorology, vol. 13 of *Atmospheric and Oceanographic Sciences Library*, Kluwer Academic Publishers, 1988.

Sørensen, J. N. and Shen, W. Z.: Numerical modeling of wind turbine wakes, Journal of Fluids Engineering, Transactions of the Asme, 124, 393–399, https://doi.org/10.1115/1.1471361, 2002.

Troldborg, N. and Andersen, S. J.: Sensitivity of Lillgrund Wind Farm Power Performance to Turbine Controller, Journal of Physics: Conference Series, 2505, 012 025, https://doi.org/10.1088/1742-6596/2505/1/012025, 2023.

van der Laan, M. P., Sørensen, N. N., Réthoré, P.-E., Mann, J., Kelly, M. C., Troldborg, N., Hansen, K. S., and Murcia, J. P.: The k-ε-fP model applied to wind farms, Wind Energy, 18, 2065–2084, https://doi.org/https://doi.org/10.1002/we.1804, 2015.

Veers, P., Dykes, K., Lantz, E., Barth, S., Bottasso, C. L., Carlson, O., Clifton, A., Green, J., Green, P., Holttinen, H., Laird, D., Lehtomäki, V., Lundquist, J. K., Manwell, J., Marquis, M., Meneveau, C., Moriarty, P., Munduate, X., Muskulus, M., Naughton, J., Pao, L., Paquette, J., Peinke, J., Robertson, A., Rodrigo, J. S., Sempreviva, A. M., Smith, J. C., Tuohy, A., and Wiser, R.: Grand challenges in the science of wind energy, Science, 366, eaau2027, https://doi.org/10.1126/science.aau2027, 2019.

Verstappen, R. W. C. P. and Veldman, A. E. P.: Symmetry-preserving discretization of turbulent flow, Journal of Computational Physics, 187, 343–368, doi:10.1016/S0021-9991(03)00126-8, 2003.

Wit, L. and van Rhee, C.: Testing an Improved Artificial Viscosity Advection Scheme to Minimise Wiggles in Large Eddy Simulation of Buoyant Jet in Crossflow, Flow, Turbulence and Combustion, 92, https://doi.org/10.1007/s10494-013-9517-1, 2013.

Wu, Y.-T. and Porté-Agel, F.: Large-eddy simulation of wind-turbine wakes: evaluation of turbine parametrisations, Boundary-layer meteorology, 138, 345–366, 2011.

Zilitinkevich, S.: Velocity profiles, the resistance law and the dissipation rate of mean flow kinetic energy in a neutrally and stably stratified planetary boundary layer, Boundary-Layer Meteorology, 46, 367–387, 1989.